

**Simon RYCKAERT**

**Nanotech**  
**Academic year 2024-2025**

**Centre de nanosciences et nanotechnologies**  
**10 Bd Thomas Gobert, 91120 Palaiseau**

# **Light-trapping in ultra-thin solar cells**

**from 01/03/2025 to 15/08/2025**



**Under the supervision of :**

- **PI : Stephane Collin and Sylvain Finot**
- **School supervisor : Anne Kaminski**

**Ecole nationale  
supérieure de physique,  
électronique, matériaux**

**Phelma**

Bât. Grenoble INP - Minatec  
3 Parvis Louis Néel - CS 50257  
F-38016 Grenoble Cedex 01

Tél +33 (0)4 56 52 91 00  
Fax +33 (0)4 56 52 91 03

**<http://phelma.grenoble-inp.fr>**

Confidentiality : no

## General introduction

Silicon remains the dominant material in the photovoltaic (PV) industry, representing over 90% of the global solar cell production. Thanks to decades of optimisation, commercial silicon cells now routinely reach power conversion efficiencies above 25%, approaching the fundamental Shockley–Queisser limit of ~29.4% for single-junction silicon cells with a thickness of 100  $\mu\text{m}$ . This limit, derived under ideal assumptions, including perfect Lambertian light scattering, places a hard ceiling on how much solar energy can be converted by a traditional silicon-based device.

To push beyond this ceiling, two main strategies have emerged. The first focuses on optical management, aiming to improve light absorption within the silicon layer. In standard thick cells, light trapping is achieved via random surface texturing, which approximates Lambertian scattering. However, this approach becomes less effective in ultra-thin silicon cells, typically below 100  $\mu\text{m}$ , where light escapes more easily due to the reduced optical path length. In this context, more advanced light-trapping schemes are needed. These include periodic nano-structures that diffract light into guided modes and quasi-random patterns that enable directional scattering, offering a controlled and broadband enhancement of absorption.

The second strategy involves stacking materials of different bandgaps to form tandem solar cells. In particular, combining a wide-bandgap top cell (e.g., III-V semiconductors or perovskites) with a silicon bottom cell allows for a more efficient use of the solar spectrum by minimising thermalisation losses, the energy wasted when high-energy photons generate carriers that quickly relax to the band edge. By allocating high-energy photons to the top cell and lower-energy ones to the silicon sub-cell, tandem architectures reduce these losses and can achieve power conversion efficiencies beyond 30%. This approach is currently one of the most promising routes for next-generation photovoltaics and is being actively pursued in both academic and industrial settings.

While both strategies, light trapping and tandem architectures, are powerful independently, their combination holds even greater potential. Ultra-thin tandem configurations not only reduce material usage and cost but also benefit significantly from effective light-trapping structures, which compensate for their reduced thickness.

This project focuses on the design, simulation, and fabrication of nano-structured light-trapping systems aimed at improving the efficiency of both single-junction and tandem silicon-based solar cells. The central goal is to investigate cost-effective and scalable nano-fabrication strategies that enhance light absorption in ultra-thin photovoltaic devices. On the simulation side, we explore periodic diffraction gratings to optimize light management in tandem architectures. Experimentally, we develop and characterise a novel class of pseudo-periodic gratings, based on self-assembled polymer blends, as a promising alternative for light trapping in the silicon bottom cell of tandem and in single-junction solar cells.

# **Table of Content**

General introduction	2
List of figures & List of Tables	4
Chapter 1 : Introduction	5
I / Basics of photovoltaic technology	5
II / Motivation and objectives	6
III / Plan of the report	6
Chapter 2 : Optical simulation of tandem solar cell	7
I / RCWA for periodic structures	7
II / Fourier orders and wavelength resolution	9
III / The Base Cell Structure Chosen for Ultra-Thin Optimisation	11
IV / Reducing absorbers thickness and adding light-trapping system	13
1. Thin top and bottom cell	13
2. Ultra-thin top and bottom cell	15
2.1. First design : dual gratings	15
2.2. Second design : Bragg Mirror (Top) & Grating (Bottom) Design	16
V/ Conclusion	17
Chapter 3 : Light trapping with quasi-random grating	18
I / Introduction	18
II / Experimental work	19
1. Process	19
1.1 Polymer blend process	19
1.2 Advanced process	20
2. Tools to analyse the polymer blend structures	21
2.1 Computation of the pseudo-period	21
2.2 Surface coverage	22
2.3 Circularity factor	23
2.4 Scattering angle	24
3. Experimental results	26
3.1 Polymer blend directly on Silicon	26
3.2 Polymer blend with advanced process	29
III / Polymer blend simulation	31
1. Physics behind the Polymer blend model	31
2. Comparison between simulation and experiments	35
IV/ Conclusion	37
Chapter 4 : Silicon Thinning	38
I / Introduction	38
II / Silicon thinning process	38
III / Experimental results	39
IV / Conclusion	41
General Conclusion	42
Appendix	43
References	44
Abstract	45
Résumé	46
Riassunto	47
Presentation of the company	48
Internship summary sheet	49

## List of figures & List of Tables

Figure 1 : Schematic of a stack of layers containing two-dimensional periodic nano-structures.....	8
Figure 2 : The baseline cell structure.....	12
Figure 3 : Thin tandem solar cell.....	14
Figure 4 : Ultra-thin/Thin tandem solar cell with double grating.....	15
Figure 5 : Ultra-thin tandem solar cell with top Bragg mirror and bottom grating.....	16
Figure 6 : Optical characteristics of the Bragg mirror.....	17
Figure 7 : The process used for creating the QR pattern.....	19
Figure 8 : Cross-section of the solar cell after removing the PMMA.....	20
Figure 9a : Fourier transform of a polymer blend 60% PS / 40 % PMMA at speed 6K RPM.....	21
Figure 9b: Radial profile of Fourier transform of a polymer blend 60%PS/40% PMMA at speed 6K RPM.....	21
Figure 10 : Binarised image of polymer blend 60% PS / 40 % PMMA at speed 6K RPM.....	23
Figure 11 : Distribution of circularities of a polymer blend 60% PS / 40 % PMMA at speed 6K RPM.....	23
Figure 12 : Angle of transmission for different wavelengths.....	25
Figure 13 : SEM images of the quasi-random patterns transferred to the Silicon layer.....	27
Figure 14 : Impact of the polymer ratio and speed of the spin-coater on the pp, ff and circularity factor.....	28
Figure 15 : 40° tilted SEM images of the quasi-random patterns transferred to the Silicon layer.....	29
Figure 16 : SEM images of the quasi-random patterns after etching SiO <sub>2</sub> .....	29
Figure 17 : Comparison simulation and experimental.....	36
Figure 18 : Comparison simulation and experimental.....	37
Figure 19 : Layout for the silicon thinning process.....	40
Figure 20 : Etched sample after 4h in the NaOH solution and 5 minutes water rinse.....	41
Figure 21 : EDX analysis of the silicon surface after 2 h 30 min of etching.....	42
Table 1 : Chosen wavelength resolution and number of Fourier modes with respect to the wavelength.....	11
Table 2 : Tested samples.....	26

# Chapter 1 : Introduction

## I / Basics of photovoltaic technology

Photovoltaic technology is based on the ability of certain materials to convert sunlight directly into electricity. This process relies on semiconductors, which have the particular property of generating charge carriers, electrons and holes, when exposed to light. When photons from the sun carry enough energy, they can excite electrons in the material, allowing them to move freely and generate an electric current. A typical solar cell is built from two layers of semiconductors with different doping types (p-type and n-type), creating an internal electric field that helps separate the generated charges and direct them toward external contacts.

To characterise a solar cell, we use several fundamental parameters. The short-circuit current density ( $J_{sc}$ ) and the open-circuit voltage ( $V_{oc}$ ) are two of them. The  $J_{sc}$ , typically expressed in mA/cm<sup>2</sup>, represents the maximum current the cell can deliver when its terminals are shorted (i.e., at zero voltage). It depends directly on how much light is absorbed and converted into charge carriers, making it highly sensitive to the optical design of the cell, carrier separation efficiency, and recombination losses. On the other hand,  $V_{oc}$  is the maximum voltage measured when no current flows (i.e., under open-circuit conditions). It reflects the ability of the device to maintain a charge carrier separation before recombination and is influenced by material quality, recombination dynamics, and the internal electric fields of the device.

These two quantities, together with the fill factor (FF), which is the ratio of the maximum power output to the product of the open-circuit voltage and short-circuit current and reflects the “squareness” of the I–V curve, determine the overall power conversion efficiency ( $\eta$ ) of the solar cell, according to the relation:

$$\eta = \frac{J_{sc} \cdot V_{oc} \cdot FF}{P_{in}}$$

where  $P_{in}$  is the incident solar power density. In practical terms, improving the efficiency of a solar cell requires simultaneously optimising  $J_{sc}$ ,  $V_{oc}$ , and FF. This can involve enhancing light absorption, e.g., by using light-trapping structures to increase  $J_{sc}$ , reducing recombination losses to raise  $V_{oc}$ , and engineering the device layout to maximise charge extraction and fill factor. Therefore, each optical and electrical improvement contributes directly or indirectly to boosting the overall efficiency of the photovoltaic device.

One of the main limitations of single-junction solar cells lies in the trade-off between absorbing high- and low-energy photons. According to the Shockley–Queisser limit, a single absorber material can only convert photons with energies above its bandgap, and the excess energy from higher-energy photons is lost as heat. This thermalisation loss limits the maximum theoretical efficiency of a single-junction silicon solar cell to around 29%. To overcome this, tandem solar cells combine two or more materials with different bandgaps, each optimised to absorb a specific part of the solar spectrum. For instance, a high-bandgap top cell (e.g., GaAs or perovskite) absorbs high-energy photons, while the lower-bandgap silicon bottom cell captures the remaining lower-energy photons. This configuration allows better spectral utilisation, reducing thermalisation losses. For two-terminals tandem solar cells (the one studied in our report), the total open-circuit voltage  $V_{oc}$  of a tandem cell is approximately the sum of the  $V_{oc}$  of the individual sub-cells while the total short circuit current  $J_{sc}$  is the minimum between the  $J_{sc}$  of the top cell and the  $J_{sc}$  of the bottom cell. As such, tandem architectures offer a compelling route to surpass the efficiency limits of single-junction technologies while making better use of the incident solar energy.

Another limitation, especially in thin-film or ultra-thin devices, is that the amount of light absorbed decreases exponentially with the absorber’s thickness. This behaviour is described by the equation:

$$A(\lambda) = 1 - e^{-\alpha(\lambda) \cdot d}$$

where  $A(\lambda)$  is the absorption at a given wavelength  $\lambda$ ,  $\alpha(\lambda)$  is the material’s absorption coefficient, and  $d$  is the thickness of the absorber layer. As this equation shows, when the thickness  $d$  is small, absorption drops significantly, especially for wavelengths where  $\alpha(\lambda)$  is low. In simple terms, thinner absorbers lead to reduced photon absorption, which directly limits the number of photo-generated carriers, and therefore lowers the short-circuit current density,  $J_{sc}$ .

To overcome this limitation, light-trapping systems are introduced. These structures aim to increase the effective optical path length of photons within the absorber without increasing its physical thickness. This can be achieved through periodic gratings, textured surfaces, or pseudo-random nano-structures that scatter or diffract light in a controlled manner. By enhancing absorption across the solar spectrum, these systems help recover, or even surpass, the  $J_{sc}$  one would obtain in thicker devices, while preserving the benefits of thin layers such as lower material consumption and potentially higher open-circuit voltage,  $V_{oc}$ . In fact, thinner devices often experience reduced recombination losses, as charge carriers have shorter distances to travel before being collected, which contributes to improving  $V_{oc}$ , another key parameter that influences the overall power conversion efficiency.

## II / Motivation and objectives

As said above, the continuous pursuit of higher efficiency and lower cost in photovoltaic technologies has led to growing interest in tandem solar cells. In parallel, making solar cells thinner opens the door to new advantages, such as reduced material consumption, lower fabrication costs, improved flexibility, and lighter modules, key features for emerging applications like integrated photovoltaics. However, thinning the absorber layers poses significant optical challenges, as less material naturally leads to reduced light absorption.

To address this, my project focuses on the development of advanced light-trapping systems designed to enhance photon absorption in both single-junction and tandem solar cells. On the simulation side, I will explore ultra-thin tandem architectures composed of an  $\text{Al}_{0.25}\text{GaAs}$  top cell and a silicon bottom cell. Using optical modeling techniques based on Rigorous Coupled-Wave Analysis (RCWA), I aim to integrate periodic gratings that enhance the short-circuit current density  $J_{sc}$  by increasing the optical path length within the absorbers.

Experimentally, I will investigate a complementary light-trapping approach based on pseudo-periodic nano-structures generated through polymer blend lithography. This technique offers a low-cost, scalable alternative to conventional patterning methods, yet poses a significantly greater challenge for numerical modelling due to the lack of strict periodicity, which prevents the use of standard simplifications such as periodic boundary conditions. In addition, the project includes the fabrication of ultra-thin silicon substrates, which are essential to the realisation of a fully integrated, ultra-thin tandem solar cell. Ultimately, this work aims to bridge numerical modelling and experimental development to contribute to next-generation high-efficiency and cost-effective photovoltaic technologies.

## III / Plan of the report

Following the motivation and objectives, the report is structured into several chapters that reflect the major axes of the work: optical simulation, nanostructure fabrication, physical modeling, and silicon thinning.

The second chapter presents the optical simulation work carried out on ultra-thin tandem solar cells. The aim is to enhance the short-circuit current by integrating periodic nano-structures. Using RCWA (Rigorous Coupled Wave Analysis), we simulate and optimize the geometry of these gratings to achieve current matching between the top and bottom subcells while maintaining high absorption. This part provides insight into the optical benefits of periodic light-trapping systems and establishes a benchmark for comparing experimental techniques.

In the third chapter, the focus shifts to the experimental development of pseudo-periodic gratings using polymer blend lithography. This low-cost and scalable method leverages the spontaneous phase separation of immiscible polymers to create nano-structures without the need for complex lithography. We describe the fabrication process, including the basic and advanced techniques used to improve the quality and reproducibility of the patterns. Various metrics, such as surface coverage, circularity, and pseudo-period, are introduced to quantitatively evaluate the structures. A simulation model based on the Cahn–Hilliard equation is also developed to better understand the phase separation mechanism, and qualitative comparisons are made with experimental results.

The fourth chapter is devoted to the thinning of silicon wafers, a crucial step in fabricating ultra-thin bottom cells for tandem solar cells. Since commercial ultra-thin silicon substrates are expensive, we explore practical methods to reduce the thickness of standard wafers down to 10 - 40  $\mu\text{m}$  while preserving their structural integrity. The challenges associated with surface roughness and mechanical stability are discussed.

Together, these chapters contribute to the broader objective of integrating efficient, cost-effective light-trapping systems into advanced photovoltaic architectures. By combining theoretical modeling, experimental fabrication, and materials engineering, this work opens promising pathways for the development of next-generation solar cells.



## Chapter 2 : Optical simulation of tandem solar cell

In this chapter, I focus on the optical simulation of an ultra-thin tandem solar cell composed of a III–V top cell and a silicon bottom cell. The objective is to optimize light absorption in both sub-cells to enhance the short-circuit current density ( $J_{sc}$ ) and achieve current matching, a critical requirement in two-terminal tandem architectures. Since the  $J_{sc}$  of the tandem cell is equal to

$$J_{sc}^{tandem} = \min(J_{sc}^{top}, J_{sc}^{bottom})$$

with  $J_{sc}^{top}$  and  $J_{sc}^{bottom}$  respectively the  $J_{sc}$  in the top sub-cell and the  $J_{sc}$  in the bottom sub cell, maximising absorption in both cells is essential. To this end, I implement and analyse two light-trapping strategies aimed at improving the optical performance and balancing the  $J_{sc}$  in both the top and bottom cells.

### I / RCWA for periodic structures

In this study, we use the program RETICOLO [1] to simulate periodic gratings. This software, written in MATLAB, is based on the Rigorous Coupled-Wave Analysis (RCWA) method, which was first developed by Moharam and Gaylord in the 1980s to analyse sinusoidally modulated holographic gratings [15]. A customised version of RETICOLO has been provided to our group.

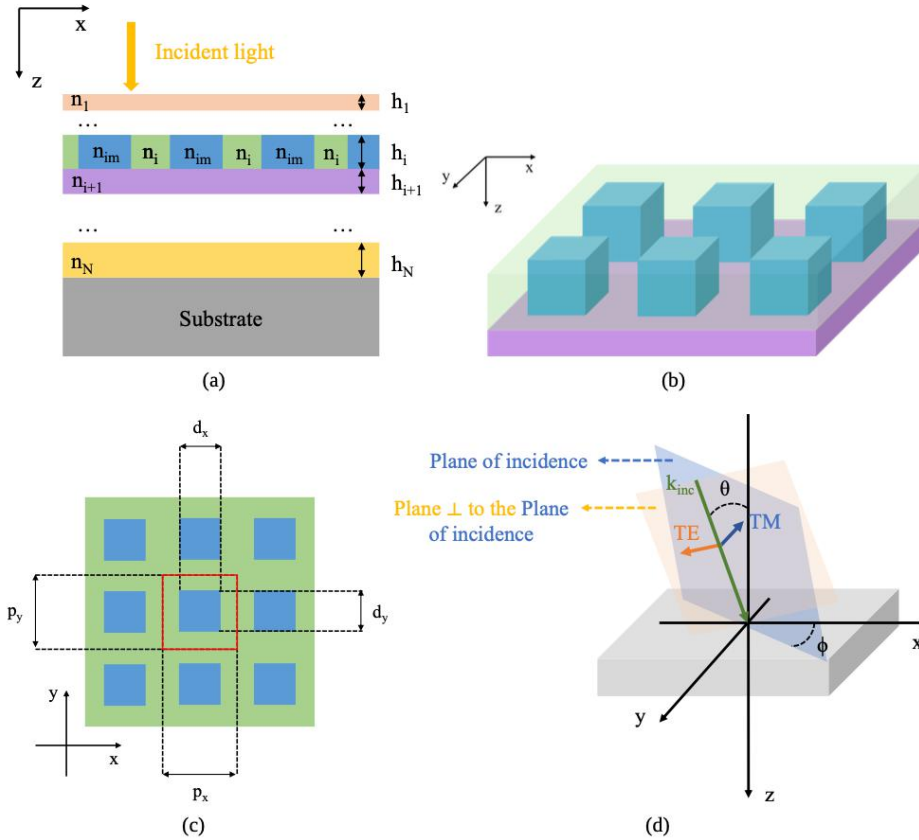


**Fig 1** : Schematic of a stack of layers containing two-dimensional periodic nano-structures used with RETICOLO to calculate the electromagnetic field inside the device. (a) Cross sectional view of the device, (b) perspective view and (c) top-view of the nano-structured layer. The red square represents a unit pattern of size  $p_x \times p_y$  on which the calculation is performed.  $p_x$  and  $p_y$  are the periods in the x and y direction respectively. The description of a period is the same in all layers of the modelled device. The nanostructure sizes are denoted  $d_x$  and  $d_y$ . (d) Schematic presentation of an incident plane wave polarised in TE and TM mode (the electric field is perpendicular or parallel to the plane of incidence). (Picture from [1])

RCWA is a semi-analytical technique that solves Maxwell's equations for a plane wave incident on a periodic structure that is assumed to be infinitely extended in the plane (x-y). The method treats the longitudinal direction (z) analytically while solving the transverse (x and y) components numerically. The grating is modelled as a multilayer system, where each layer consists of periodic inclusions (with refractive index  $n_{im}$ ) embedded in a matrix material (with refractive index  $n_i$ ). In our case, each layer shares the same periodicity ( $p_x = p_y$ ) and inclusion size ( $d_x = d_y$ ), forming a regular square pattern. The surface coverage is defined as  $ff = \frac{d_x d_y}{p_x p_y}$ , and structures are centered within the period to preserve symmetry and improve numerical performance.

All simulations in this work are performed under normal incidence using a square mesh for spatial discretization with an axis of symmetry along  $x = y$ , where TE and TM polarizations produce similar results. The azimuthal angle is set to zero ( $\Phi = 0$ ).

RETICOLO discretises each layer in the z-direction, and expands the in-plane (x, y) dielectric function  $\epsilon_r(x, y)$  into a Fourier series:

$$\epsilon_r(x, y) = \sum_{m=-\infty}^{\infty} \sum_{n=-\infty}^{\infty} \hat{\epsilon}_r(m, n) \exp \left[ 2i\pi \left( \frac{mx}{p_x} + \frac{ny}{p_y} \right) \right] \quad (1)$$

The electromagnetic fields are also expressed in this Fourier basis, leading to a coupled system of linear differential equations that can be formulated as an eigenvalue problem. The number of Fourier modes retained in the x and y directions ( $M_x, M_y$ ) directly affects the size of the matrix, which is  $2 \times (2M_x + 1) \times (2M_y + 1)$ , and the accuracy of the simulation. A trade-off between computational cost and convergence must therefore be considered.

In the vertical (z) direction, the fields are expanded using a Rayleigh basis in the homogeneous regions above and below the grating. The mode amplitudes are then computed recursively by enforcing boundary conditions across interfaces, using a scattering matrix formalism. This allows full reconstruction of the electromagnetic field throughout the structure. Quantities such as total reflection, transmission, and layer-resolved absorption can be calculated, including the power dissipated in each layer via Poynting's theorem.

Because RCWA represents the fields using plane waves, it is especially efficient for periodic structures with low to moderate refractive index contrast [1].

To calculate the short-circuit current density  $J_{sc}$  using RCWA method, we first determine the wavelength-dependent absorption  $A(\lambda)$  of the active layer and then integrate it over the solar spectrum. The relation used is:

$$J_{sc} = q \int_{\lambda_{min}}^{\lambda_{max}} A(\lambda) \Phi(\lambda) d\lambda$$

where:

- $A(\lambda)$  is the absorption at wavelength  $\lambda$ , representing the fraction of incident photons absorbed by the layer.
- $\Phi(\lambda)$  is the incident solar photon flux density (in  $photons \cdot m^{-2} \cdot s^{-1} \cdot nm^{-1}$ ) at wavelength  $\lambda$ .
- $q$  is the elementary charge ( $1.602 \times 10^{-19}$  C).

In our simulations, we assume an internal quantum efficiency (IQE) of 1, which means every absorbed photon generates one collected electron contributing to the current, so there is a direct proportionality between absorbed photons and collected charge carriers.



The solar photon flux  $\Phi(\lambda)$  is calculated from the solar spectral irradiance  $S(\lambda)$  (in  $W \cdot m^{-2} \cdot nm^{-1}$ ), which for standard testing is taken as the AM1.5G spectrum:

$$\Phi(\lambda) = \frac{S(\lambda)}{E(\lambda)} = \frac{S(\lambda) \cdot \lambda}{hc}$$

With :

- $S(\lambda)$  is the solar spectral irradiance at wavelength  $\lambda$ ,
- $h$  is Planck's constant,
- $c$  is the speed of light in vacuum,
- $E(\lambda) = \frac{hc}{\lambda}$  is the energy of a single photon at wavelength  $\lambda$ .

This conversion from spectral irradiance to photon flux takes into account that only photons with energy above the semiconductor bandgap contribute to carrier generation: each such photon generates a single electron-hole pair, with any excess energy lost to thermalisation. Photons with energy below the bandgap are not absorbed and do not produce current. Therefore, the relevant photon flux is the number of photons per unit area per unit time at each wavelength that can generate charge carriers.

The integration limits are selected based on the material properties and solar spectrum:

- The lower wavelength limit is typically set to  $\lambda_{\min} = 300$  nm, since solar photon flux below this value is negligible due to atmospheric absorption and solar intensity.
- The upper wavelength limit corresponds roughly to the bandgap wavelength of silicon  $\lambda_{\max} \approx 1200$  nm (bandgap energy  $\sim 1.1$  eV), since photons with wavelengths longer than this are not absorbed and do not contribute to the photocurrent.

Putting it all together, the short-circuit current density is calculated as:

$$J_{sc} = q \int_{300 \text{ nm}}^{1200 \text{ nm}} A(\lambda) \frac{S(\lambda) \cdot \lambda}{hc} d\lambda \quad (2)$$

This expression quantifies the maximum possible current generated assuming perfect charge collection and no recombination losses other than those implied by absorption.

## II / Fourier orders and wavelength resolution

As discussed previously, both the accuracy and computational time of RCWA simulations depend strongly on the number of Fourier modes  $M_x$  and  $M_y$ . If an insufficient number of modes is used, the simulation may not converge, leading to unphysical or misleading results. However, increasing the number of modes excessively can cause the computational time to grow significantly, due to the size of the resulting eigenvalue problem. Therefore, selecting appropriate values for  $M_x$  and  $M_y$  is essential to maintain a balance between accuracy and efficiency.

In the case of homogeneous layers only, the number of Fourier modes has no impact on the results. Since there are no guided or diffracted modes and light propagates according to Snell's law, the structure can be modelled accurately with  $M_x = M_y = 0$ . However, when gratings or structured layers are present, more Fourier orders are necessary to capture the light scattering and mode coupling properly, especially in high-index-contrast systems.

This issue becomes particularly significant during optimisation, where thousands of simulations are required to scan parameter space. If a single simulation takes several minutes, optimising over thousands of configurations can become computationally prohibitive.

To manage simulation time while ensuring sufficient accuracy during the optimisation of the tandem structure composed of an  $Al_{0.25}GaAs$  top cell and a silicon bottom cell, I adopted a wavelength-dependent choice of Fourier modes. Since convergence is generally more difficult for silicon than for III-V materials, and given that  $Al_{0.25}GaAs$  absorbs most of the light below  $\sim 750$  nm (bandgap  $\approx 715$  nm), I used the following strategy:

- For wavelengths between 300 and 750 nm, where light is absorbed in the top cell due to a single pass through the material, I used  $M_x = M_y = 5$ .
- For 750 - 900 nm, where the light begins to interact more with the silicon layer but is still far from its bandgap, I increased the modes to  $M_x = M_y = 10$ .
- For 900 - 1200 nm, near the silicon bandgap where convergence is most difficult, I used  $M_x = M_y = 15$  to ensure accuracy.

Another important parameter is the wavelength resolution, i.e., the spectral step size between two adjacent simulation points. In RCWA, the spectrum is discretised, and reducing the number of points can save time. However, this must be done carefully. If the absorption spectrum contains narrow peaks (e.g., due to resonances), a coarse wavelength step may entirely miss these features, leading to incorrect estimates of  $J_{sc}$ .

To address this, the wavelength resolution was also adapted depending on the spectral range: where the spectrum varies slowly, larger steps were used during optimisation to reduce computation time. However, in regions with rapid spectral changes, finer resolution was maintained. This parameter must be chosen with care, perhaps even more so than the number of Fourier modes, as it can easily introduce non-physical results if set improperly. The wavelength resolutions used in each case are summarised in Table 1, where Steps denotes the spacing between two consecutive wavelength points.

To validate the accuracy of the results after optimisation, each optimised structure was re-simulated using  $M_x = M_y = 15$  across the entire wavelength range and a wavelength resolution of 1 nm.

Wavelength (nm)	Steps (nm)	Number of Fourier modes ( $M_x = M_y$ )
300 - 750	5	5
750 - 900	2	10
900 - 1250	2	15

**Tab 1** : Chosen wavelength resolution and number of Fourier modes with respect to the wavelength when having a tandem cell composed of a  $Al_{0.25}GaAs$  top cell and a Silicon bottom cell with grating for both top and bottom cell. Those values are for optimisation steps.

### III / The Base Cell Structure Chosen for Ultra-Thin Optimisation

In the following sections, I focus on the optimisation approach used to improve the performance of the ultra-thin tandem solar cell structure. Before presenting the specific results, it is important to clarify what is meant by “optimizing the structure” in this context, and to explain the methodology employed.

When we talk about optimizing the tandem solar cell, the goal is to find the optimal set of parameters, here, the thicknesses, materials of the different layers and potentially the grating parameters, that maximize the device’s  $J_{sc}$ . Since this is a multi-layered thin-film structure, the parameters of each layer directly influences the optical interference effects, absorption profile, and ultimately the short-circuit current density ( $J_{sc}$ ) generated in each subcell.

To tackle this optimization problem, I use MATLAB’s surrogate optimization function. This algorithm is particularly useful when the objective function is computationally expensive or with complex landscapes characterized by numerous local minima, as is the case when calculating  $J_{sc}$  through electromagnetic simulations like RCWA. Each evaluation requires simulating light absorption across the entire solar spectrum and determining the current generated, which is time-consuming.

The surrogate optimization works by first sampling the objective function at a set of initial points in the design space. Using these points, it builds a computationally cheap approximate model, a “surrogate”, which predicts the objective function’s behavior. The algorithm then uses this surrogate to identify promising areas to explore further. By iteratively refining the surrogate model and selectively sampling new points, the algorithm converges toward an optimal solution with fewer expensive evaluations compared to exhaustive search methods.

In our specific case, the objective function takes as input a vector representing the parameters of the layers composing the tandem cell structure. The active layers are predefined when creating the structure, so the simulation specifically calculates the short-circuit current densities ( $J_{sc}$ ) generated in these designated top and bottom active layers. Because the tandem’s total current is limited by the smaller of the two subcells’ currents, due to their series electrical connection, the output of the objective function is defined as:

$$J_{sc} = \min(J_{sc}^{top}, J_{sc}^{bottom}) \quad (3)$$

Finally, since the surrogate optimization algorithm is designed to minimize the objective function, we multiply  $J_{sc}$  by -1. This allows the algorithm to maximize the tandem’s current by minimizing the negative of the current. Through this approach, the optimization algorithm efficiently identifies the thickness configuration that leads to the highest current-limited  $J_{sc}$ .

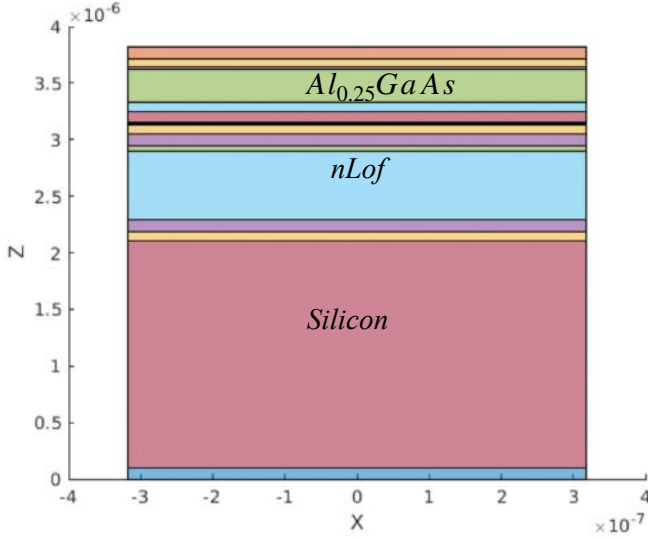
Now that the optimization method has been explained in detail, in the following sections I will simply refer to “optimizing the structure” without repeatedly specifying that surrogate optimization is used. We can now focus on presenting and analyzing the results.

The baseline tandem solar cell structure selected for ultra-thin optimisation is presented in Figure 2. Before introducing light-trapping features such as gratings or reducing the thickness of the absorber layers, namely the  $\text{Al}_{0.25}\text{GaAs}$  top cell and the silicon bottom cell, the focus was placed on optimising the anti-reflective coating (ARC) and double-layer anti-reflective coating (DLARC) systems. The Top DLARC layers are designed to minimise reflection at the air/tandem interface, where the refractive index mismatch is significant, while the DLARC layers are introduced to reduce reflection at the interface between the top or bottom cells and the intermediate bonding layers (composed of PEDOT and nLOF).

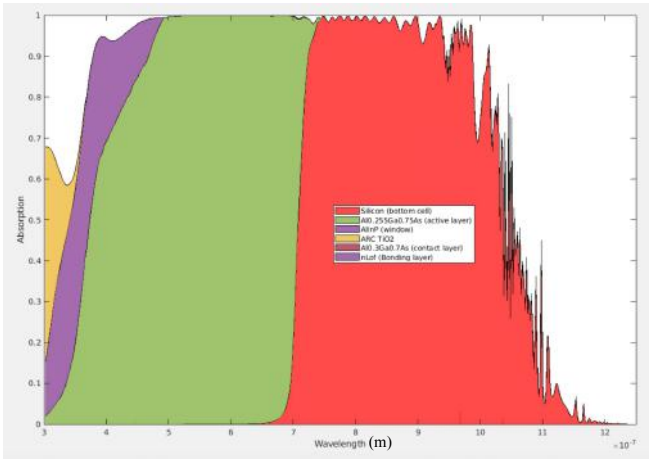
The structure includes two ARC layers (Top DLARC1 and Top DLARC2) on the front side and four DLARC layers (DLARC1–DLARC4) embedded within the bonding regions. These six layers were optimised in thickness and material to minimise reflection and maximise absorption. The thicknesses shown in Figure 2 correspond to the values obtained after numerical optimisation. During this process, the thickness of each Top DLARC and DLARC layer was allowed to vary between 0 and 200 nm, and each layer could be composed of ITO,  $\text{TiO}_2$ ,  $\text{MgF}_2$ , or  $\text{SnO}_2$ , which are materials with varied refractive indices and optical properties commonly used for anti-reflective applications.

Interestingly, the optimisation revealed that a full DLARC configuration was not necessary for this particular structure. In fact, the optimal configuration involved a reduced number of layers, as DLARC2 and DLARC3 converged to 0 nm, indicating that a single-layer ARC on each interface was sufficient to minimise reflection losses. This simplified structure not only reduces fabrication complexity but also leads to excellent optical

performance, achieving a short-circuit current density ( $J_{sc}$ ) of 19.5 mA/cm<sup>2</sup> in both the top and bottom cells, thus ensuring current matching, a crucial requirement in two-terminal tandem architectures.



(a)



(c)

Layers	Thickness
<b>MgF2 (Top DLARC 1)</b>	<b>105 nm</b>
<b>TiO2 (Top DLARC 2)</b>	<b>50 nm</b>
AlInP (Window)	25 nm
Al <sub>0.25</sub> GaAs (Absorber)	2620 nm
Al <sub>0.6</sub> GaAs (BSF)	75 nm
Al <sub>0.3</sub> GaAs (Contact)	100 nm
GaAs (Contact)	10 nm
<b>ITO (DLARC 1)</b>	<b>92 nm</b>
<b>MgF2 (DLARC 2)</b>	<b>0 nm</b>
PEDOT (Gluing layer)	100 nm
nLof (Gluing layer)	5700 nm
<b>MgF2 (DLARC 3)</b>	<b>0 nm</b>
<b>TiO2 (DLARC 4)</b>	<b>82 nm</b>
Silicon (Absorber)	250 $\mu$ m
Ag (back mirror)	Semi - infinite

(b)

**Fig 2** : The baseline cell structure. (a), the cross section of the structure, (b), Table detailing the materials, purposes, and thicknesses of the layers, listed in the same top-to-bottom order as they appear in the cross-sectional view, (c), the absorption spectrum of the cell. Optimised layers are shown in bold in (b).

## IV / Reducing absorbers thickness and adding light-trapping system

In this section, the goal is to reduce the thickness of the absorber layers in the tandem solar cell, specifically the  $\text{Al}_{0.25}\text{GaAs}$  top cell and the silicon bottom cell, to move toward an ultra-thin design without compromising too much performance. The approach is divided into two phases. First, I investigate how much the thicknesses of both absorbers can be reduced without significant loss in short-circuit current density ( $J_{sc}$ ), in order to assess the thickness limits beyond which optical performance degrades. Second, I explore strategies to intentionally thin down the tandem structure, aiming to find an optimal trade-off between device thickness and optical efficiency.

A central challenge in ultra-thin tandem solar cells lies in maintaining high absorption, especially in the top cell, while reducing material usage. Unlike single-junction architectures where a grating is typically placed above a back mirror to diffract and reflect light back into the absorber, this configuration is not directly transferable to the top cell of a tandem. In a tandem structure, longer wavelengths need to transmit through the top cell to reach the silicon bottom cell. As such, the top cell must include light-trapping mechanisms that enhance absorption without relying on a back reflector that would block light from reaching the bottom cell.

To address this, I propose and compare two light-trapping strategies for the top cell: (i) introducing a nano-structured diffraction grating, and (ii) integrating a Bragg mirror to selectively reflect shorter wavelengths while allowing longer wavelengths to pass through. These designs aim to enhance light confinement in the top cell, enabling ultra-thin architectures while maintaining current matching and high overall efficiency.

### 1. Thin top and bottom cell

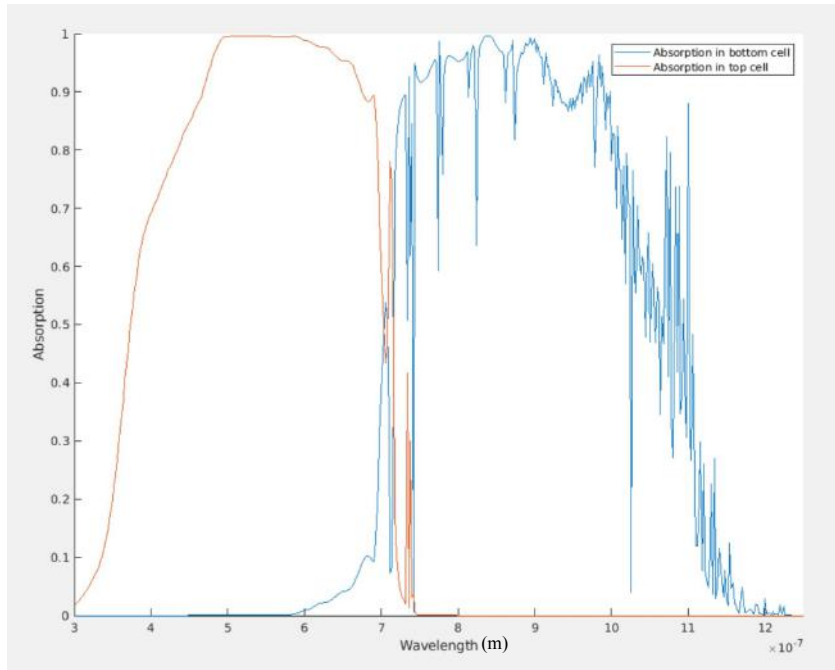
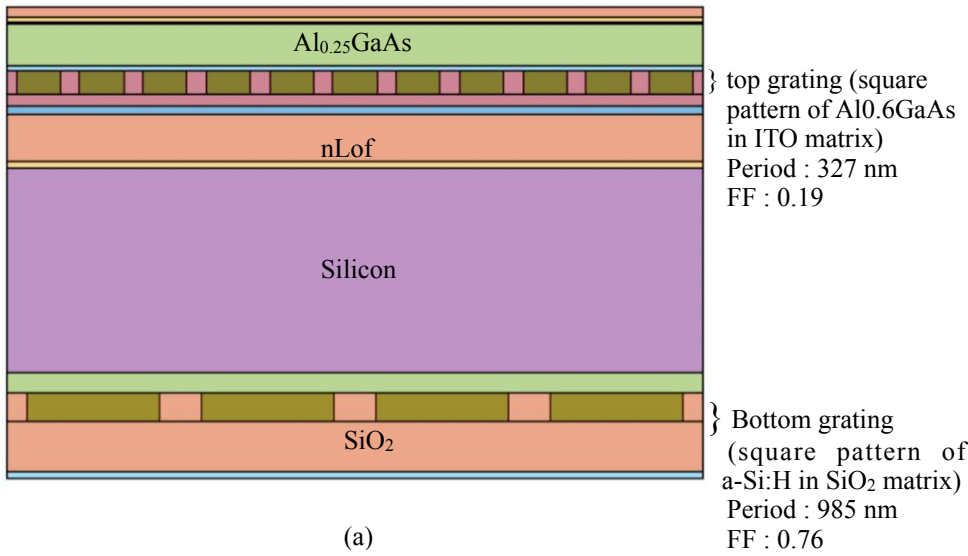
In this section, I focus on reducing the thickness of the tandem solar cell as much as possible without significantly compromising the short-circuit current density ( $J_{sc}$ ). To enhance light absorption despite thinner absorbers, I introduced periodic gratings on both the top and bottom cell of the device, as illustrated in Figure 3a. Each grating is characterised by three key parameters: period, height (which corresponds to the thickness of the grating layer), and surface coverage (SC). These parameters, along with the spacer layers thickness, were treated as free variables during the optimisation process.

As a result of this optimisation, I successfully reduced the  $\text{Al}_{0.25}\text{GaAs}$  top cell thickness from 2620 nm to 1000 nm and the silicon bottom cell thickness from 250  $\mu\text{m}$  to 80  $\mu\text{m}$ , while still maintaining strong absorption in both sub-cells. The corresponding absorption spectra are shown in Figure 3c, yielding  $J_{sc}$  values of 19.3  $\text{mA}/\text{cm}^2$  and 19.4  $\text{mA}/\text{cm}^2$  for the top and bottom cells, respectively, demonstrating effective current matching even with significantly reduced material usage.

One key challenge in simulating this configuration lies in the use of two gratings with different periods, which breaks the assumption of strict periodicity required by RCWA (Rigorous Coupled-Wave Analysis). To address this, there are two main approaches:

1. Super-period method: One can define a common super-period such that the periods of both gratings are integer divisors of it (i.e., super-period =  $a \times$  top grating period =  $b \times$  bottom grating period, with  $a, b \in \mathbb{N}$ ). This ensures global periodicity and compatibility with RCWA. However, this method can impose strict constraints on the choice of grating periods and leads to large computational domains, significantly increasing simulation time.
2. Sequential simulation method (used in this work): The structure is split into two sub-simulations. First, the top cell is simulated alone, and both its absorbed and transmitted light spectra are calculated. Then, the transmitted specular spectrum from the top cell is used as the input illumination for the bottom cell simulation. This modular approach bypasses the periodicity constraint and allows each grating to be independently optimised.

This method provides a practical solution for modeling non-proportional dual-grating structures while maintaining high optical fidelity, making it particularly useful for thin/ultra-thin tandem designs that rely on distinct grating strategies in the top and bottom cells.



Layers	Thickness
MgF2 (Top DLARC 1)	105 nm
TiO2 (Top DLARC 2)	50 nm
AlInP (Window)	25 nm
Al <sub>0.25</sub> GaAs (Absorber)	1000 nm
Al <sub>0.6</sub> GaAs (BSF)	75 nm
<b>Top grating</b>	<b>240 nm</b>
<b>ITO (ARC + Top Spacer)</b>	<b>57 nm</b>
PEDOT (Gluing layer)	100 nm
nLof (Gluing layer)	5700 nm
TiO2 (ARC)	82 nm
Silicon (Absorber)	80 $\mu$ m
Amorphous Silicon	250 nm
<b>Bottom grating</b>	<b>350 nm</b>
<b>SiO2 (Bottom spacer)</b>	<b>420 nm</b>
Ag (back mirror)	Semi - infinite

(b)

**Fig 3** : Thin tandem solar cell. (a), the cross section of the structure, (b), Table detailing the materials, purposes, and thicknesses of the layers, listed in the same top-to-bottom order as they appear in the cross-sectional view, (c), the absorption spectrum of the cell. Optimised layers are shown in bold in (b).

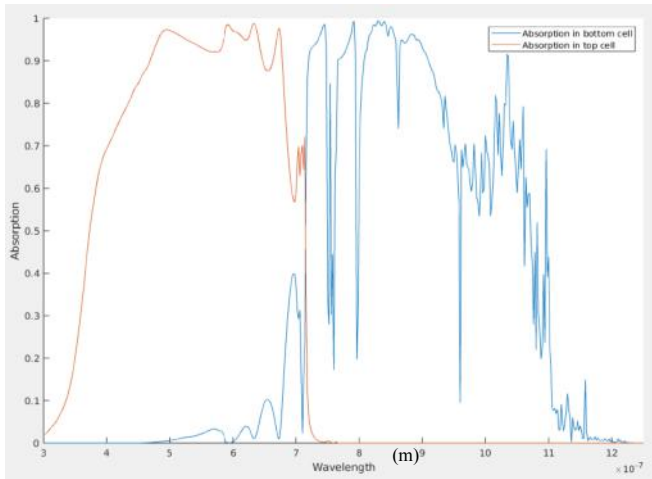
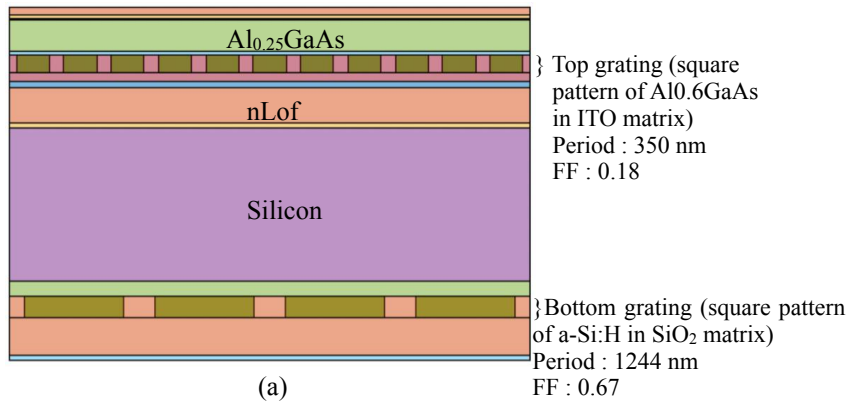


## 2. Ultra-thin top and bottom cell

In this section, the goal is to push the tandem solar cell design toward ultra-thin configurations by further reducing the thickness of both absorber layers. Based on a Pareto optimisation, the  $\text{Al}_{0.25}\text{GaAs}$  top cell thickness was fixed at 500 nm, as reducing it beyond this point leads to a sharp drop in  $J_{sc}$ , breaking the near-linear trade-off between thickness and absorption. The silicon bottom cell thickness is then minimised as much as possible while maintaining current matching with the top cell. To enhance light absorption in the thinner top absorber, I explore and compare two light-trapping strategies: using a grating or integrating a Bragg mirror beneath the top cell.

### 2.1. First design : dual gratings

In this approach, as in the previous section, I employ two separate gratings, one for the top cell and one for the bottom cell. The resulting optimised structure is shown in Figure 4.a. With this configuration, using a 500 nm thick  $\text{Al}_{0.25}\text{GaAs}$  absorber, I achieved a  $J_{sc}$  of 18.5 mA/cm<sup>2</sup> in the top cell. I manage to reduce the silicon absorber to 50  $\mu\text{m}$  while maintaining the current matching. Reducing the silicon thickness further would break the current balance unless the top cell's  $J_{sc}$  is also lowered, which would compromise overall performance. One of the key limitations of this structure is that the top grating struggles to function as a spectral filter, it does not sufficiently transmit longer wavelengths to the bottom cell while reflecting the shorter ones for efficient absorption in the top cell. This limits its effectiveness in ultra-thin tandem configurations where spectral selectivity is critical.



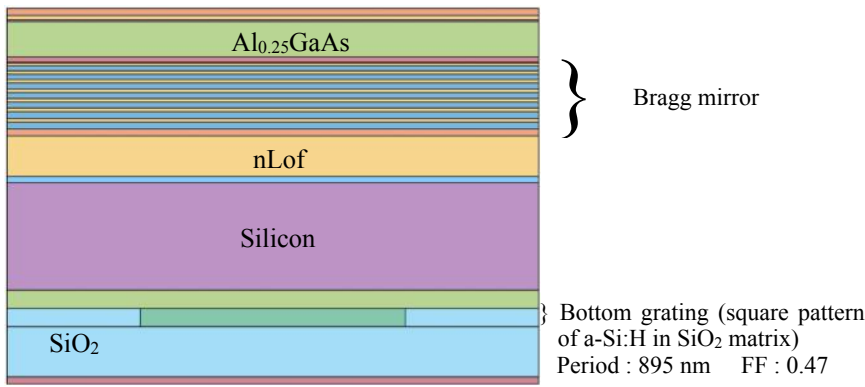
Layers	Thickness
MgF2 (Top DLARC 1)	105 nm
TiO2 (Top DLARC 2)	50 nm
AlInP (Window)	25 nm
$\text{Al}_{0.25}\text{GaAs}$ (Absorber)	500 nm
$\text{Al}_{0.6}\text{GaAs}$ (BSF)	75 nm
<b>Top grating</b>	<b>360 nm</b>
<b>ITO (ARC + Top Spacer)</b>	<b>107 nm</b>
PEDOT (Gluing layer)	100 nm
nLof (Gluing layer)	5700 nm
TiO2 (ARC)	82 nm
Silicon (Absorber)	50 $\mu\text{m}$
Amorphous Silicon	250 nm
<b>Bottom grating</b>	<b>454 nm</b>
<b>SiO2 (Bottom spacer)</b>	<b>852 nm</b>
Ag (back mirror)	Semi - infinite

**Fig 4 :** Ultra-thin/Thin tandem solar cell with double grating. (a), the cross section of the structure, (b), Table detailing the materials, purposes, and thicknesses of the layers, listed in the same top-to-bottom order as they appear in the cross-sectional view, (c), the absorption spectrum of the cell. Optimised layers are shown in bold in (b).

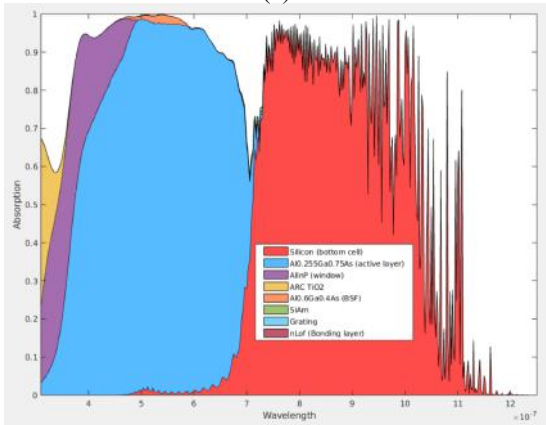
The peaks observed in Fig. 4c (blue) between 750 nm and 900 nm are caused by the top grating reflecting these wavelengths. These photons are not absorbed by the top cell because their energies are below its bandgap.

## 2.2. Second design : Bragg Mirror (Top) & Grating (Bottom) Design

To improve spectral selectivity between short and long wavelengths, a Bragg mirror was used as the top light-trapping system instead of a grating. The Bragg mirror, intended to function as a wavelength filter, consists of seven pairs of alternating  $\text{TiO}_2$  and  $\text{SiO}_2$  layers with variable thicknesses. Seven pairs were chosen as the optimal compromise between achieving good spectral selectivity and keeping the number of layers manageable for easier fabrication. It was optimised to reflect short-wavelength light back into the top cell while allowing longer wavelengths to reach the bottom cell. The optimised structure is shown in Figure 5.a. As in the previous method, the  $\text{Al}_{0.25}\text{GaAs}$  absorber thickness was fixed at 500 nm, and the optimisation aimed to maximise the top-cell  $J_{sc}$ . Once the top-cell performance was set, the silicon layer thickness was reduced until current matching was restored. With this design, a matched  $J_{sc}$  of  $17.8 \text{ mA/cm}^2$  was achieved in both sub-cells, and the silicon thickness was successfully reduced to  $15 \mu\text{m}$ . In this configuration, the top cell is clearly the limiting factor: as seen in the absorption spectrum (Figure 5.b), a dip around 700 nm indicates that while light at these wavelengths is effectively reflected by the Bragg mirror, the  $\text{Al}_{0.25}\text{GaAs}$  layer is too thin to absorb it efficiently. Unlike gratings, the Bragg mirror does not diffract light, but thanks to its excellent filtering properties (Figure 6) , it enables a significant reduction in silicon thickness without compromising current matching.



(a)



(c)

Layers	Thickness
MgF2 (Top DLARC 1)	105 nm
TiO2 (Top DLARC 2)	50 nm
AlInP (Window)	25 nm
$\text{Al}_{0.25}\text{GaAs}$ (Absorber)	500 nm
$\text{Al}_{0.6}\text{GaAs}$ (BSF)	75 nm
<b>TiO2/SiO2 (Bragg mirror)</b>	<b>795 nm</b>
<b>ITO (ARC + Top Spacer)</b>	<b>107 nm</b>
PEDOT (Gluing layer)	100 nm
nLof (Gluing layer)	5700 nm
TiO2 (ARC)	82 nm
Silicon (Absorber)	$15 \mu\text{m}$
Amorphous Silicon	250 nm
<b>Bottom grating</b>	<b>318 nm</b>
<b>SiO2 (Bottom spacer)</b>	<b>842 nm</b>
Ag (back mirror)	Semi - infinite

(b)

**Fig 5** : Ultra-thin tandem solar cell with top Bragg mirror and bottom grating. (a), the cross section of the structure. (b), Table detailing the materials, purposes, and thicknesses of the layers, listed in the same top-to-bottom order as they appear in the cross-sectional view. (c), the absorption spectrum of the cell. Optimised layers are shown in bold in (b)

Figure 6 shows the optical characteristics of the Bragg mirror. We observe that wavelengths above 700 nm are almost entirely transmitted through the mirror, allowing them to reach the bottom cell. Between 500 and 700 nm, the light is almost completely reflected back toward the top cell, enhancing absorption in this spectral range. For wavelengths below 500 nm, the reflection is not complete; however, this is not an issue since the top cell absorbs nearly all of this light on the first pass, as confirmed in Figure 5.b, so very little reaches the Bragg mirror in that range.

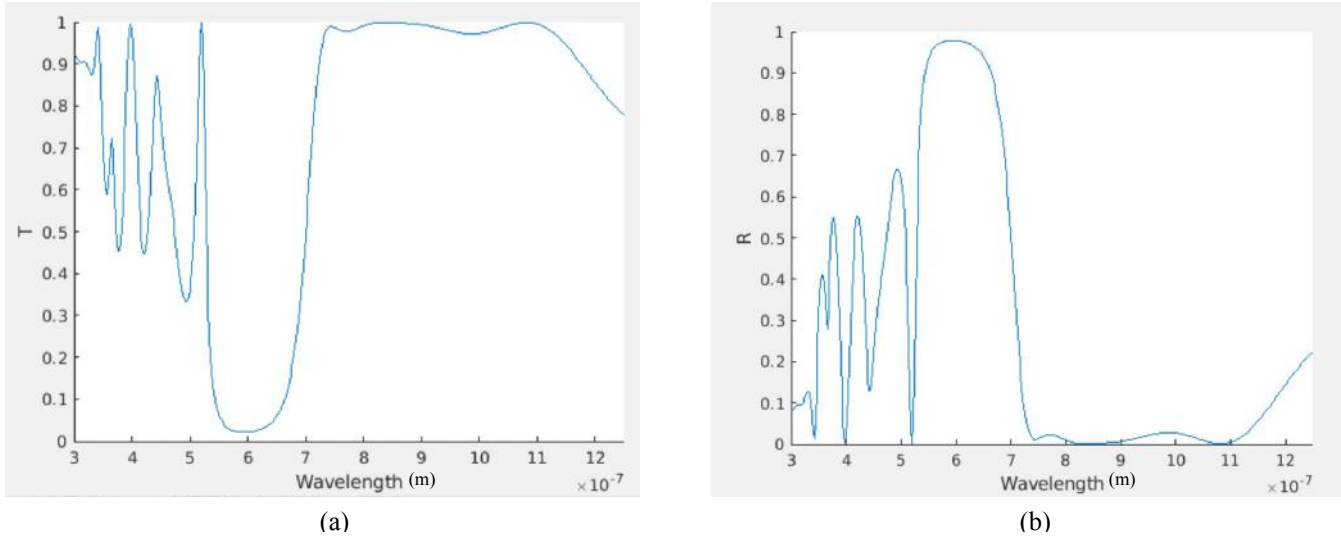


**Fig. 6:** Optical characteristics of the Bragg mirror with a semiconductor layer ( $n = 3.5$ ) on top and a resin/polymer substrate ( $n = 1.5$ ) underneath. (a) Transmission spectrum of the Bragg mirror. (b) Reflection spectrum.

## V/ Conclusion

In this chapter, we explored different strategies to reduce the thickness of the absorbers in a tandem solar cell composed of an  $\text{Al}_{0.25}\text{GaAs}$  top cell and a silicon bottom cell, while maintaining efficient current matching between the two sub-cells. By first optimising anti-reflective coatings (ARC and DLARC), we established a baseline structure capable of achieving balanced photocurrents. We then investigated two light-trapping approaches to further thin down the absorbers: using gratings on both sub-cells, or combining a Bragg mirror for the top cell with a grating for the bottom cell.

The dual-grating configuration enabled a significant reduction of both absorber layers, 500 nm for the  $\text{Al}_{0.25}\text{GaAs}$  top cell and 50  $\mu\text{m}$  for the silicon bottom cell, while maintaining a high photocurrent ( $J_{\text{sc}} = 18.5 \text{ mA/cm}^2$ ). However, the top grating exhibited limited spectral filtering capabilities, which constrained further reduction of the silicon thickness. In contrast, the Bragg mirror-based design offered superior spectral selectivity, enabling a more aggressive thinning of the silicon layer down to 15  $\mu\text{m}$ . This came at the cost of a slightly lower  $J_{\text{sc}}$  in the top cell (17.8  $\text{mA/cm}^2$ ), due to insufficient absorption of the top cell. For comparison, achieving the same  $J_{\text{sc}}$  with the dual-grating approach would require a 500 nm  $\text{Al}_{0.25}\text{GaAs}$  layer and a 25  $\mu\text{m}$  thick silicon layer.

These results underscore the critical balance between light trapping and spectral filtering in the development of ultra-thin tandem solar cells. Specifically, they reveal that above a certain photocurrent threshold, corresponding to the maximum  $J_{\text{sc}}$  achievable in the top cell with a Bragg mirror for a given top absorber thickness, the dual-grating approach becomes more effective, as it allows for higher overall photocurrent while maintaining current matching. However, below this threshold, the Bragg mirror configuration proves more advantageous, as its superior spectral selectivity enables a greater reduction in the thickness of the silicon bottom cell without compromising current matching. This makes the Bragg mirror method particularly well suited for applications where ultra-lightweight and compact devices are prioritised (e.g., space-based photovoltaics or flexible electronics), while the dual-grating design is more appropriate when maximising efficiency is the primary objective.

## Chapter 3 : Light trapping with quasi-random grating

### I / Introduction

As photovoltaic technologies move toward ever thinner absorber layers in order to reduce material consumption and fabrication costs, efficient light-trapping strategies have become essential to compensate for the reduced optical path length. In the previous section, we explored the use of periodic photonic gratings to enhance light absorption in ultra-thin solar cells. These structures, based on repeating patterns, can efficiently couple incident light into guided modes and increase absorption through diffraction. However, their fabrication often relies on high-precision lithographic processes, which are not always scalable or cost-effective.

In this part, we investigate an alternative light-trapping method based on the self-assembly of polymer blends, which allows the formation of quasi-random (or pseudo-periodic) nano-structures without the need for expensive lithography. The method consists of mixing two immiscible polymers such as polystyrene (PS) and polymethyl methacrylate (PMMA) in a common solvent (PGMEA). By spin-coating the mixture onto a substrate and making the solvent evaporate, the system undergoes phase separation driven by spinodal decomposition. This results in the formation of nanoscale domains rich in either polymer A or B, whose morphology can be tuned by varying the spin-coating speed, polymer ratio, molar mass of polymers and solution concentration.

Once the desired morphology is achieved, one of the polymers is selectively removed using a wet etchant, leaving behind a disordered but statistically controlled pattern. This pattern can then be transferred into a semiconductor material, such as silicon in our case, by using the remaining polymer as a mask in an etching step. The resulting structure acts as a pseudo-periodic grating, able to directionally scatter light over a broad spectral range. Compared to periodic gratings, these structures offer several advantages: cheaper and faster to fabricate.

This method, commonly referred to as polymer-blend lithography, has been shown to produce photonic structures with high scattering power spectral density [2], enabling efficient light-trapping in ultra-thin absorbers. In contrast to purely random roughening or deterministic periodicity, quasi-random structures combine the best of both worlds: a rich distribution of spatial frequencies to cover a broad spectral range, and a high degree of local order that enhances scattering efficiency.

In the following section, I present the principles of this technique, its implementation in our study, and how it could be simulated. We detail the influence of processing parameters on the resulting morphology and demonstrate how such self-assembled structures can be used to fabricate cost-effective light-trapping layers for ultra-thin photovoltaic devices.

## II / Experimental work

### 1. Process

#### 1.1 Polymer blend process

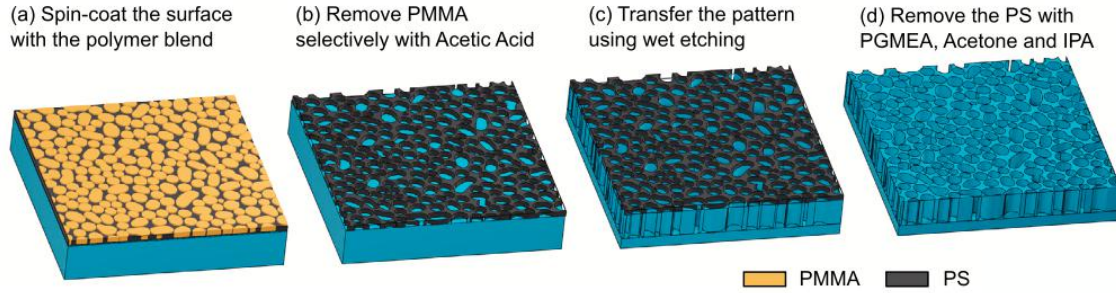


**Fig 7 :** The process used for creating the QR pattern. (a) Surface after the spin coating solution with islands of PMMA (b) Surface after removing the PMMA using acetic acid, (c) the pattern transfer to the Silicon using dry etching, (d) removal of the PS with PGMEA, acetone and IPA. (Picture from [2])

In this study, we employed polymer blend lithography to fabricate pseudo-periodic light-trapping structures on silicon substrates. This method leverages the phase separation of two immiscible polymers (polystyrene (PS) and polymethyl methacrylate (PMMA)) to create nano-structured masks without requiring high-resolution lithographic tools.

Both polymers were chosen with identical molar masses of 100 kg/mol to ensure comparable viscoelastic properties and promote well-defined phase separation during solvent evaporation. In the future, we expect to change those molar masses to observe the impact on the polymer blend morphology. Two precursor solutions were prepared independently by dissolving 0.1 g of PS and 0.1 g of PMMA in 4 g of propylene glycol monomethyl ether acetate (PGMEA), a common solvent compatible with both polymers and widely used in standard lithographic processes. These precursor solutions were then mixed at a defined weight ratio depending on the target morphology. The final ratio was selected based on the mass fraction of each polymer; for instance, a 50:50 blend corresponds to equal masses of PS and PMMA in the final mixture. This ratio governs the resulting domain geometry, from isolated PS islands to interconnected PMMA networks, consistent with phase-separation behaviour described by the Cahn–Hilliard framework [11].

The polymer blend solution was spin-coated onto the substrate at a fixed acceleration of 2000 RPM/s. The spin speed was the variable parameter considered in our study, as it directly influences the solvent evaporation rate and feature size of the resulting microstructure. After spin-coating, the sample was baked at 130 °C for 12 minutes to promote evaporation of the remaining solvent and “freeze” the phase-separated morphology.

To create a selective mask, PMMA was removed using a simple wet-etching process: the sample was immersed in acetic acid for 3 minutes, followed by a gentle rinse in deionized water for 1 minute without agitation. This step selectively dissolved PMMA domains, leaving behind a PS-only pattern on the silicon surface.

The PS mask was then used to transfer the pattern into the underlying silicon via Inductively Coupled Plasma Reactive Ion Etching (ICP RIE) using a C<sub>4</sub>F<sub>8</sub>, Ar, SF<sub>6</sub> gas mixture. The depth of the etched grating is determined by the etch duration and the selectivity of the process between PS and silicon. In our case, the PS layer was approximately 50 nm thick, which limited the maximum achievable grating depth to about 250 nm before the mask was fully consumed. To overcome this limitation and extend the etching depth without sacrificing lateral resolution, we deposited a thin SiO<sub>2</sub> buffer layer prior to the polymer blend process.



## 1.2 Advanced process

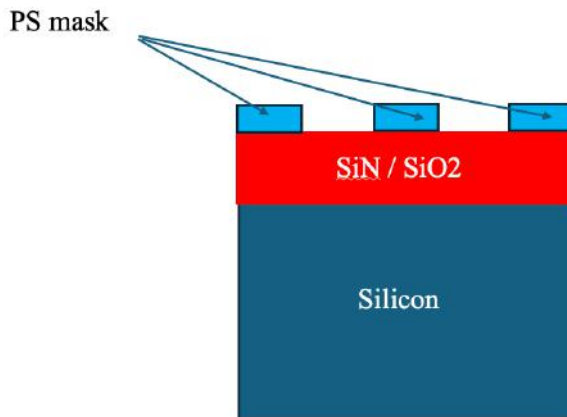


**Fig 8 :** Cross-section of the solar cell after removing the PMMA  
( before dry etching steps)

As mentioned previously, one of the key limitations when directly using a PS polymer mask to etch nano-structures into a silicon substrate lies in the thickness of the PS mask. Due to the relatively fast consumption of the polymer under plasma etching conditions, the maximum achievable etch depth is typically restricted to approximately five times the initial PS thickness.

To address this issue, we incorporated an additional processing step in which a thin layer of silicon dioxide ( $\text{SiO}_2$ ) is deposited onto the silicon surface prior to the polymer blend lithography. The PS/PMMA blend is then deposited and processed directly on top of this  $\text{SiO}_2$  layer. The idea behind this approach is that  $\text{SiO}_2$  offers a much higher etch selectivity against silicon compared to PS. This means that once the PS pattern is transferred into the  $\text{SiO}_2$  via plasma etching, the more robust  $\text{SiO}_2$  structures can serve as a durable hard mask for further etching into the silicon, allowing us to reach greater depths without compromising pattern fidelity.

A 100 nm  $\text{SiO}_2$  layer was initially deposited using a sol-gel process for testing, though alternative deposition methods could be explored later. A silica precursor solution composed of tetraethyl orthosilicate (TEOS), HCl, ethanol and triethoxymethylsilane was spin-coated at 3000 RPM for 30 seconds, using an acceleration of 3000 RPM/s. The resulting thin film was then annealed two times first at 120°C for 2 min then at 330 °C for 10 minutes on a hot plate to ensure full evaporation of residual solvent.

Once the  $\text{SiO}_2$  layer is deposited on the silicon substrate, the polymer blend lithography process described earlier is applied on top of it. After spin-coating the PS/PMMA blend, thermally fixing the morphology, and removing the PMMA via selective wet etching, a first RIE step is then carried out to transfer the PS pattern into the underlying  $\text{SiO}_2$  layer. After this etch, the residual PS is removed by sequential rinses in acetone and isopropanol (IPA), leaving behind a patterned  $\text{SiO}_2$  hard mask that faithfully replicates the initial PS morphology.

A second ICP-RIE process is then employed to etch the silicon substrate using the  $\text{SiO}_2$  mask. Since  $\text{SiO}_2$  exhibits high resistance under these conditions, the etch can proceed much deeper into the silicon without mask degradation. As a result, we should be able to achieve targeted grating depths in the range of 400 to 1000 nm, depending on the duration and plasma parameters used in this second etching step.



## 2. Tools to analyse the polymer blend structures

In order to understand and optimize the structures obtained through polymer blend lithography, it is essential to develop dedicated analysis tools capable of quantifying their morphological and optical properties. Unlike periodic gratings, pseudo-periodic or quasi-random patterns generated by phase separation are inherently disordered and require specific metrics to characterise them effectively. To this end, we implemented a series of numerical and image-processing tools to extract key parameters such as the average pseudo-period (or characteristic length scale), the surface coverage, their shape circularity, and the expected scattering angles associated with the observed spatial frequencies. These tools are crucial not only for monitoring fabrication reproducibility, but also for linking processing conditions such as spin speed or polymer ratio to the final optical performance of the grating structures.

### 2.1 Computation of the pseudo-period

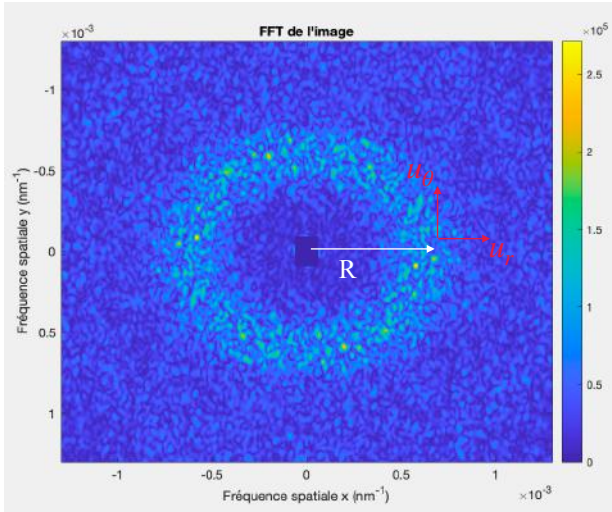


**Fig 9.a :** Fourier transform of a polymer blend 60% PS / 40 % PMMA at speed 6K RPM

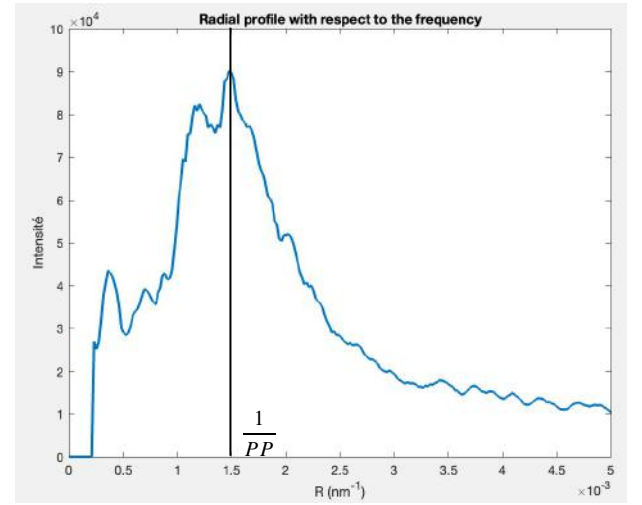


**Fig 9.b :** Radial profile of Fourier transform of a polymer blend 60% PS / 40 % PMMA at speed 6K RPM

Despite the absence of strict periodicity, these morphologies often exhibit a degree of short-range order characterised by a dominant length scale, the so-called pseudo-period (pp). This quantity can be seen as the average center-to-center distance between domains rich in either polymer A or B, and plays a crucial role in determining the diffraction behaviour and light-scattering properties of the resulting structure.

To extract this pseudo-period quantitatively, we analyse the two-dimensional Fourier transform of top-view SEM images of the polymer blend pattern. In the Fourier domain, a perfectly periodic structure would give rise to discrete Bragg peaks, whereas a pseudo-periodic structure manifests as a continuous ring of intensity centered at the origin ( Figure 9.a ). The presence of this ring reflects the isotropic distribution of a dominant spatial frequency in real space. In the image of the structure in the Fourier domain, I hide the continuous component (center) to observe the ring better.

To compute the pseudo-period, we first perform an angular integration of the Fourier amplitude, effectively collapsing the 2D spectrum into a 1D radial profile. We are able to do that due to the angular symmetry of the ring (i.e., the invariance of intensity with respect to the angle  $\theta$ ).

$$I(R) = \frac{1}{2\pi} \int_0^{2\pi} |F(R, \theta)| d\theta \quad \text{with } F(R, \theta) \text{ the Fourier transform of the pseudo-grating}$$

The resulting radial profile exhibits a pronounced peak corresponding to the dominant spatial frequency  $f_\mu$ , from which the pseudo-period  $\Lambda$  is simply calculated as:  $\Lambda = \frac{1}{f_\mu}$

This method is illustrated in Figure 9.a and Figure 9.b, where the ring structure and its radial profile are clearly visible. A broader peak indicates incomplete statistical sampling, which may result either from a higher degree of morphological disorder or from the use of an image window that is too small to capture the representative structural features. Therefore, both the peak width and the radial symmetry of the ring serve as indicators of the quality and statistical representativeness of the pattern.

## 2.2 Surface coverage

The surface coverage (SC) is a key morphological parameter that quantifies the fraction of the surface area occupied by one of the polymer phases, typically the domains of PS after selective removal of PMMA. While the pseudo-period provides information about the average spacing between adjacent domains, the surface coverage describes how much of the total surface is actually covered by these domains, offering insight into their relative size and packing density.

To calculate the surface coverage, we analyse binarised images of the polymer blend pattern, typically obtained from SEM or optical microscopy. In these processed images, each pixel is classified as either belonging to a blob (foreground) or the surrounding matrix (background). The surface coverage is then simply defined as the ratio:

$$SC = \frac{N_{\text{blobs}}}{N_{\text{total}}} \quad (4)$$

where  $N_{\text{blobs}}$  is the number of pixels corresponding to the “blobs” domain, and  $N_{\text{total}}$  is the total number of pixels in the image. This approach assumes a uniform scale across the image and provides a dimensionless number between 0 and 1, representing the area fraction of blob on the surface.

The surface factor is particularly useful when comparing different spin-coating conditions or polymer ratios, as it reflects how the phase separation dynamics translate into physical domain sizes. A higher surface coverage generally corresponds to larger blobs domain, while a lower surface coverage may indicate smaller or more sparsely distributed domains. Combined with the pseudo-period, the surface coverage allows for a more complete morphological characterisation of the polymer blend pattern and helps anticipate its impact on light scattering.

### 2.3 Circularity factor

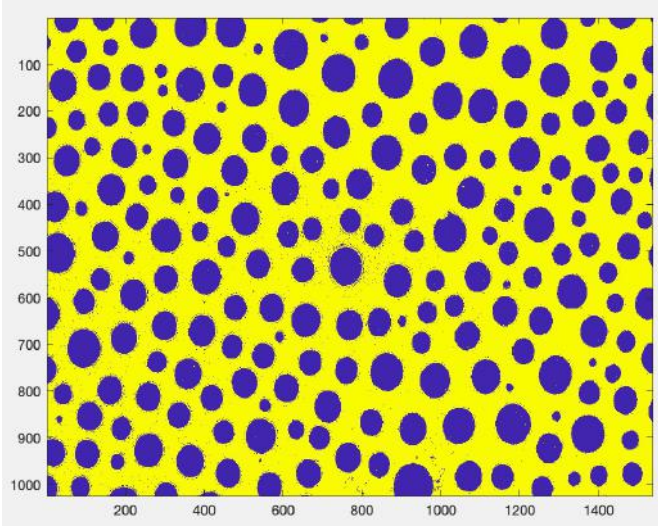


**Fig 10 :** Binarised image of polymer blend 60% PS / 40 % PMMA at speed 6K RPM

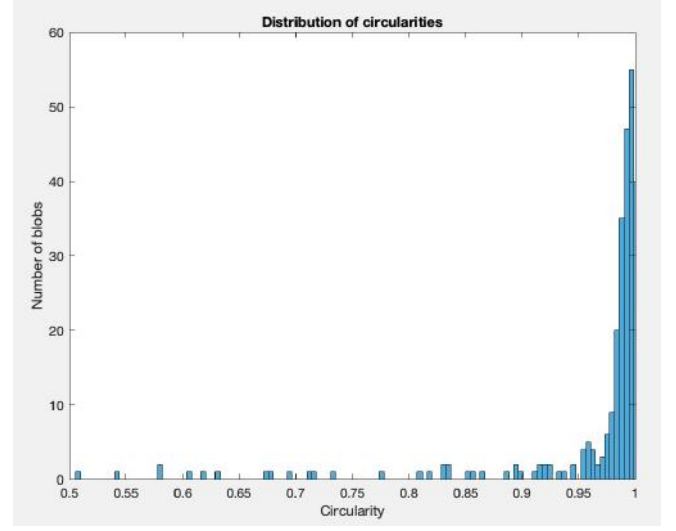


**Fig 11:** Distribution of circularities of a polymer blend 60% PS / 40 % PMMA at speed 6K RPM

To further characterise the morphology of the polymer blend pattern, we introduced a circularity factor to evaluate the shape of the blobs formed after phase separation. When performing polymer blend lithography, the domain shape can vary significantly depending on parameters such as the PS:PMMA ratio, ranging from nearly circular isolated islands to elongated or interconnected structures.

The circularity of a given domain  $i$  is defined as:  $C_i = \frac{4\pi A_i}{P_i^2}$  (5)

where  $A_i$  is the area and  $P_i$  the perimeter of the  $i^{\text{th}}$  domain. This dimensionless ratio takes a maximum value of 1 for a perfect circle, which minimises the perimeter for a given area. As the shape becomes more irregular, elongated, or branched, the circularity decreases.

To compute these values, we first apply a binarization algorithm to the grayscale SEM images in order to distinguish the blobs domain from the background. However, due to imperfections in the thresholding process, small artefacts or “impurities” may appear in the binary image, typically as isolated pixels or small clusters incorrectly classified. These non-physical features can bias shape descriptors like circularity or fill factor.

To address this, we implemented a cleaning algorithm that removes such pixels by filtering out connected components below a defined size threshold. An example of these artefacts is visible in Figure 10 before cleaning. After processing, only well-defined domains are retained for analysis, ensuring that the calculated circularity factors reflect the actual morphology of the blobs.

Finally, we compute the circularity factor for each identified domain and represent the distribution as a histogram (see Figure 11). This statistical overview allows us to compare the domain shapes across different fabrication conditions and better understand the transition between droplet-like and interconnected morphologies.

## 2.4 Scattering angle

To evaluate the light-scattering properties of the pseudo-periodic structures fabricated via polymer blend lithography, it is important to estimate the scattering angle associated with a given spatial frequency. In our case, although the grating is not strictly periodic, we can approximate its dominant spatial frequency using the pseudo-period ( $\Lambda$ ), extracted from Fourier analysis (see previous section). This pseudo-period acts similarly to the pitch of a periodic grating and allows us to derive the angular dispersion of diffracted light.

We begin by considering an incident plane wave of wavelength  $\lambda$ , propagating in the incident medium of refractive index  $n_i$ . The wave number in the incident medium is:

$$k_0 = \frac{2\pi}{\lambda} = \frac{2\pi n_i}{\lambda_0}$$

We assume normal incidence, so the incident wave vector  $\vec{k}_i$  is aligned with the z-axis:  $\vec{k}_i = k_0 \hat{u}_z$ . The scattered wave vector  $\vec{k}_{\text{sca}}$  must have the same magnitude as  $\vec{k}_i$ , due to energy conservation:  $\|\vec{k}_{\text{sca}}\| = k_0$ . Meanwhile, the grating introduces an in-plane spatial wave vector  $\vec{k}_\mu$ , which in our isotropic case is expressed in polar coordinates (since there is no angular dependence):

$$\vec{k}_\mu = \frac{2\pi}{\Lambda} \hat{u}_r$$

with  $\hat{u}_r$  a radial unit vector in the xy-plane. Applying the boundary condition of tangential wave vector conservation at the grating interface:

$$\vec{k}_{\text{sca}, //} = \vec{k}_{i, //} + \vec{k}_\mu$$

Since the incident wave is normal to the surface, its in-plane component is zero:  $\vec{k}_{i, //} = 0$ , so:  $\vec{k}_{\text{sca}, //} = \vec{k}_\mu$ . Now, decompose  $\vec{k}_{\text{sca}}$  into its in-plane and vertical components:

$$\vec{k}_{\text{sca}} = \vec{k}_{\text{sca}, //} + \vec{k}_z = \vec{k}_\mu + \vec{k}_z$$

Taking the square of the norm (since  $\vec{k}_\mu \perp \vec{k}_z$ , the cross term vanishes) :

$$k_0^2 = \|\vec{k}_\mu\|^2 + \|\vec{k}_z\|^2$$

This leads to:

$$\cos(\theta_{\text{sca}}) = \frac{k_z}{k_0} = \sqrt{1 - \left( \frac{\|\vec{k}_\mu\|}{k_0} \right)^2} \Rightarrow \theta_{\text{sca}} = \arcsin \left( \frac{\|\vec{k}_\mu\|}{k_0} \right)$$

Substituting  $\|\vec{k}_\mu\| = \frac{2\pi}{\Lambda}$  and  $k_0 = \frac{2\pi n_i}{\lambda_0}$ , we obtain:

$$\theta_{\text{sca}} = \arcsin \left( \frac{\lambda_0}{\Lambda n_i} \right) \quad (6)$$

This angle corresponds to the direction in which the scattered wave propagates within the incident medium. To ensure physical propagation (i.e., avoid evanescent modes), the argument of the arcsin must be  $\leq 1$ . Therefore, for a given wavelength  $\lambda_0$ , a scattering condition is satisfied only if:

$$\lambda_0 < \Lambda \cdot n_i$$

This condition defines the cut-off wavelength, beyond which the mode becomes evanescent and does not contribute to light trapping.

Once the scattering angle  $\theta_{\text{sca}}$  in the incident medium (e.g., air) is known, we can use Snell's Law to compute the transmission angle  $\theta_m$  in the substrate (e.g., silicon). Assuming the refractive indices of the incident and transmitted media are  $n_i$  and  $n_t$  respectively:

$$n_i \sin(\theta_{\text{sca}}) = n_t \sin(\theta_m)$$

Using our expression for  $\theta_{\text{sca}}$  (6), this yields:

$$\theta_m = \arcsin\left(\frac{\lambda_0}{\Lambda \cdot n_t}\right) \quad (7)$$

This final expression provides the means to predict the angles at which a given wavelength can propagate within the substrate, based only on geometric and optical constraints. However, the presence of such allowed propagation angles does not guarantee that significant optical energy will be coupled into all of them. The actual angular distribution of energy depends on factors such as the diffusion efficiency of the pseudo grating and the coupling conditions.

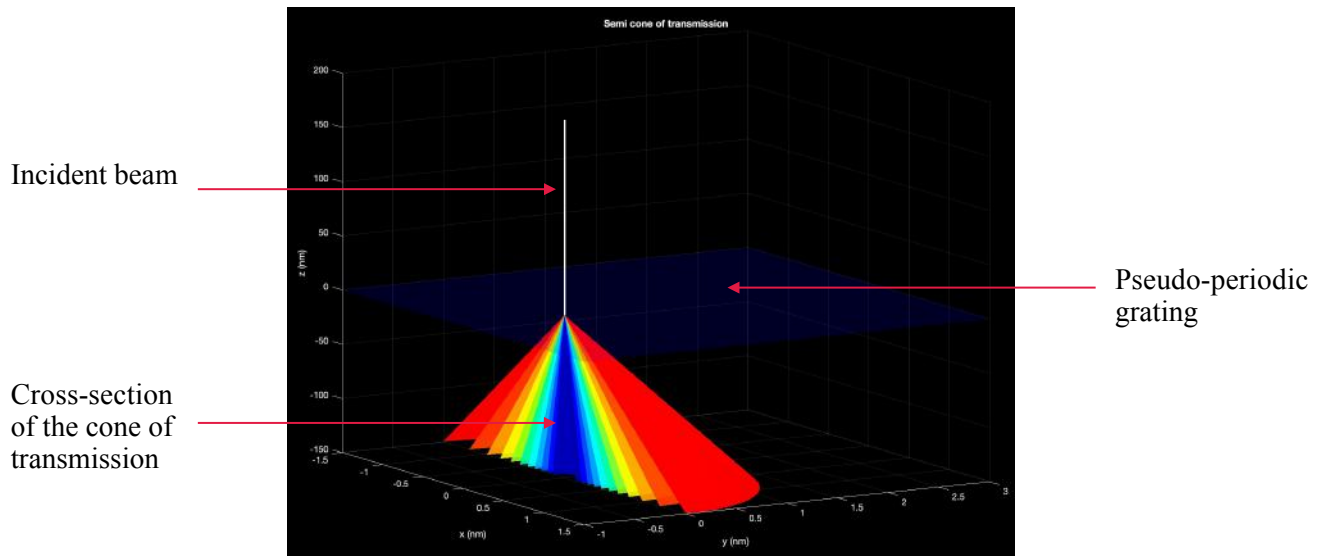


**Fig 12 : Angle of transmission for different wavelengths**

### 3. Experimental results

In this section, I present the experimental investigations carried out using polymer blend lithography. The work is divided into two main parts: the first focuses on the direct application of the polymer blend process onto silicon substrates, while the second explores the use of an intermediate SiO<sub>2</sub> layer, as previously described in the process section.

The objective of this experimental study was twofold. First, to gain deeper insight into the physical behaviour of phase separation in polymer blends under various processing conditions, such as spin speed and polymer ratio, and second, to evaluate the feasibility and limitations of this technique in producing well-defined grating structures. Key characteristics such as domain morphology, pseudo-period, grating depth, and structural uniformity were systematically analysed in order to assess the potential of polymer blend lithography for light-trapping applications in ultra-thin solar cells.

#### 3.1 Polymer blend directly on Silicon

		Mass ratio PS / PMMA				
		30/70	40/60	50/50	60/40	70/30
Spin-coater speed (RPM)	3000					
	5000					
	6000					

**Tab 2 :** Tested samples. White cells = tested cells

For the polymer blend directly on silicon, I investigated a range of processing conditions by systematically varying two key parameters: the spin-coating speed and the polymer weight ratio (PS:PMMA). A matrix of tested conditions is summarised in the table above. In this matrix, each cell represents a unique combination of spin speed and polymer ratio. White cells indicate the conditions that were experimentally tested, while black cells correspond to combinations that were not explored during this study. This structured approach allowed for a clear evaluation of how each parameter influences the resulting morphology, such as domain size, pseudo-period, and pattern uniformity.

This parametric study revealed that both spin speed and polymer ratio have a significant impact on the resulting domain morphology (Figure 13). At moderate PS:PMMA ratios (e.g., 50:50, 60:40 or even 30:70), we consistently observed the formation of well-separated polymer-rich domains with clear contrast, which are suitable for mask transfer. However, for the PS:PMMA 70:30 ratio, I was unable to obtain any usable phase-separated structures, regardless of the spin speed. The morphology either showed poorly defined domains, or an absence of visible contrast, making these samples unsuitable for further processing.

The absence of clear phase separation at high PS content raises questions about the underlying mechanism. While experimental limitations such as solubility mismatch or kinetic trapping during spin-coating could contribute, a more detailed understanding requires insight into the thermodynamic and dynamic behaviour of the polymer blend. This is what motivated the development of a simulation model presented in the next section, which aims to reproduce and explain such morphological transitions using a diffusion model. These simulations provide valuable clues as to why certain polymer ratios fail to generate usable structures and help identify regimes that are more favourable for controlled pattern formation.



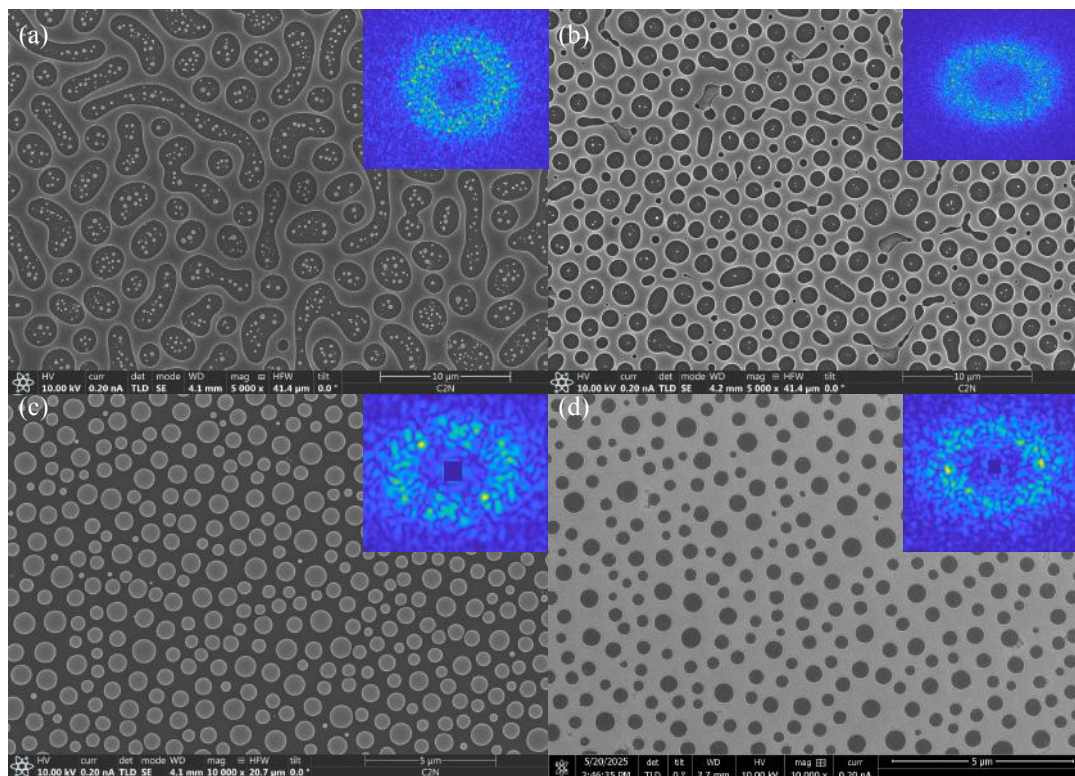


**Fig 13:** SEM images of the quasi-random patterns transferred to the Silicon layer in (a),(b),(c) and not transferred in (d) ; inset: FFT of image to define the average lattice parameter . The PB is spin-coated at 6K rpm, the polymer mass ratio PS/PMMA is 50/50 (a), 60/40 (b), 40/60 (c), 30/70 (d)

The morphology of the polymer blend patterns is highly sensitive to the polymer composition, with significant changes in domain shape, surface coverage, and pseudo-period observed across different PS:PMMA ratios. As the ratio deviates further from 50:50, the system tends to produce more circular, well-isolated domains of the minority phase. This trend is consistent with classical phase-separation behaviour, where asymmetric compositions lead to droplet-in-matrix morphologies, as opposed to the bicontinuous structures typically observed near symmetric blends. As a result, both the surface coverage and the pseudo-period decrease with increasing asymmetry, since the minority domains become smaller and more sparsely distributed (Figure 14).

Interestingly, the spin-coating speed does not appear to significantly influence the domain shape or the surface coverage. Instead, it primarily affects the scale of the pattern, effectively shrinking the morphology without altering its topology. This observation is consistent with the idea that higher spin speeds produce thinner films and faster solvent evaporation, thereby freezing the phase-separation process at an earlier stage, leading to smaller domain sizes but similar structural patterns.

One particularly noteworthy result is the apparent inversion symmetry between the 60:40 and 40:60 polymer compositions. In principle, these two systems should produce complementary patterns, where the majority and minority phases switch roles. While this behaviour is qualitatively observed, the inversion is not perfectly symmetric. A subtle asymmetry persists, which may be attributed to differences in viscosity, interaction parameters, or evaporation kinetics between PS- and PMMA-rich mixtures. Such asymmetry can be linked to kinetic effects and slight differences in the solubility of each polymer in the solvent.

These observations highlight the importance of finely tuning the polymer ratio and processing conditions in order to control the resulting pattern morphology, especially when targeting specific surface coverage or grating types for optical applications.

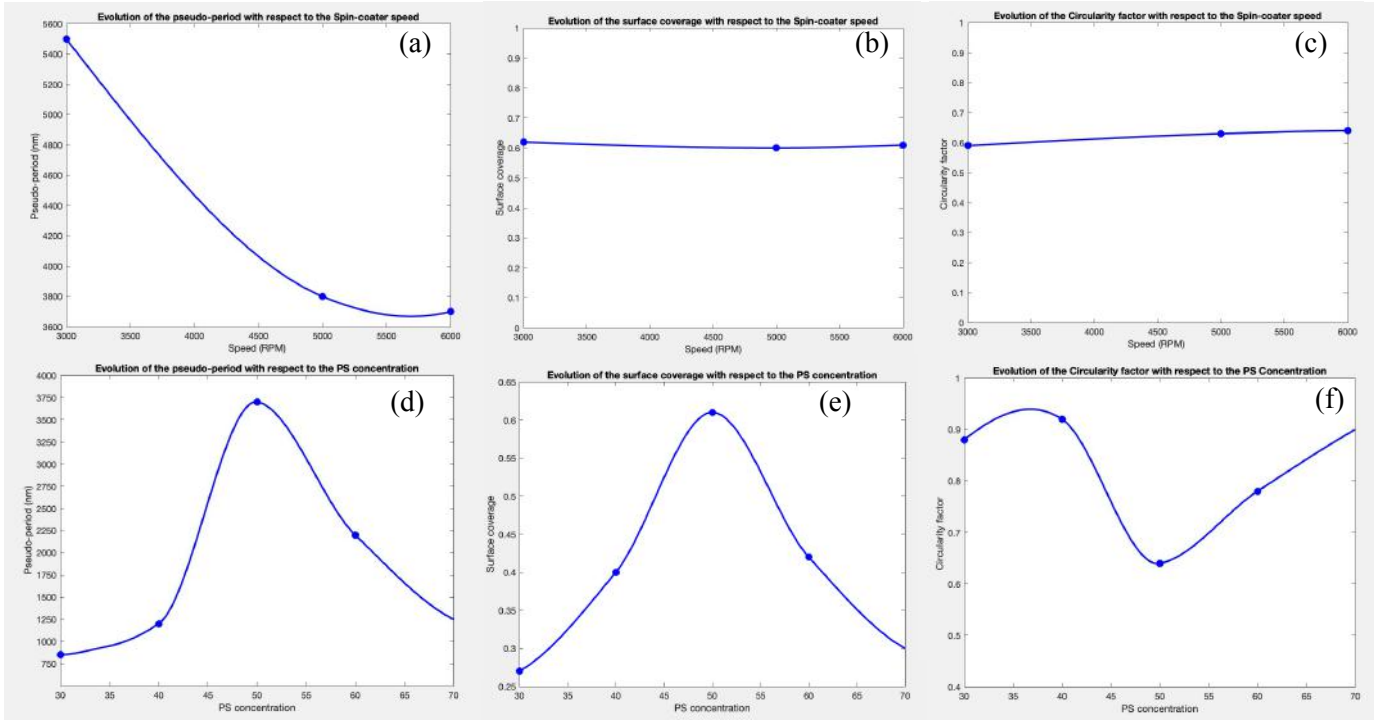


**Fig 14 :** Impact of the polymer ratio and speed of the spin-coater on the pseudo-period, surface coverage and circularity factor. Spin-coater speed is 6000 RPM for (d),(e),(f). PS concentration is 50% in mass for (a), (b), (c). Solid lines are guides for the eyes

Although Figure 14 lacks precision due to the limited number of data points in each plot, it still reveals several noteworthy trends. Most notably, the asymmetry with respect to PS concentration is clearly visible, reinforcing the observation that polymer blend morphology is not perfectly symmetric around the 50:50 ratio. We also observe this phenomenon for different conditions. Additionally, the influence of spin-coating speed on various morphological parameters such as pseudo-period and domain size is evident, even if the sparse data limits detailed quantitative analysis.

To assess the third dimension of the silicon grating, its etching depth, we performed a 4-minute dry etch using a plasma composed of  $\text{SF}_6$ ,  $\text{C}_4\text{F}_8$  and Ar (ICP - RIE) on samples fabricated with different polymer ratios. As shown in (Figure 15), the etching process completely consumed the PS mask, resulting in structures with an average depth of approximately 250 nm, regardless of the polymer ratio or lateral feature size.

Interestingly, we observe that the etch depth remains constant across a wide range of domain sizes, which may seem counterintuitive at first. One might expect that larger polymer droplets, due to their increased volume or curvature, would offer more resistance to the plasma and result in deeper etched features. However, this hypothesis is not supported by the experimental data. For instance, with a 40:60 PS:PMMA ratio, we observe ~250 nm deep features with blobs diameter around 500 nm (Figure 15b), while the 60:40 sample, containing larger blobs around 1  $\mu\text{m}$ , also yields structures of the same depth. Even in the 50:50 blend, where domain diameters reach up to 3–4  $\mu\text{m}$ , the etched depth remains limited to ~250 nm.

This observed uniformity in etch depth suggests that the PS mask has a uniform thickness across the sample, rather than forming droplet-like profiles with significant height variations. Despite the differences in lateral domain size, the mask acts as a flat, consistent etch barrier, leading to similar etch depths throughout.

Importantly, once the PS is fully consumed, the etching process does not stop; instead, the plasma begins to etch the exposed silicon at a uniform rate, causing the entire patterned structure to shift downwards. This effect can be observed over a reasonable time, as the etching recipe has been specifically designed to maintain strong anisotropy. Nevertheless, it confirms the need for a more robust hard mask (such as  $\text{SiO}_2$ , as discussed earlier) when deeper etching is required.

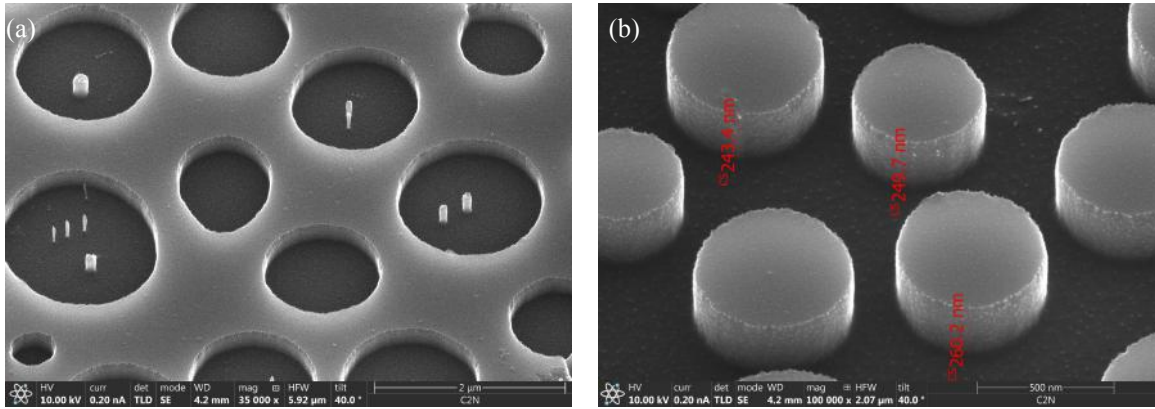


**Fig 15** : 40° tilted SEM images of the quasi-random patterns transferred to the Silicon layer. The PB is spin-coated at 6K rpm, the polymer mass ratio PS/PMMA is 60/40 (a), 40/60 (b)

### 3.2 Polymer blend with advanced process

In this part of the study, I applied the advanced fabrication process introduced earlier, which incorporates a spin-coated  $\text{SiO}_2$  layer as a hard mask beneath the polymer blend. The purpose of this approach was twofold. First, I aimed to determine whether the substrate material, specifically transitioning from bare silicon to a silicon dioxide surface, has any influence on the morphology of the phase-separated polymer blend.

This concern was motivated by findings from [2], in which the polymer blend lithography process was performed on GaAs substrates. While they reported similar qualitative morphologies to those observed in my experiments on silicon, the resulting structures were significantly smaller in scale. For instance, their 50:50 PS:PMMA ratio produced a pseudo-period of around  $1\ \mu\text{m}$ , whereas in my case, the same ratio yielded structures with pseudo-periods of  $3\text{--}4\ \mu\text{m}$ . This observation raised the question of whether the change of substrate could influence the final morphology of phase separation.

Although the difference between silicon and  $\text{SiO}_2$  is expected to be much smaller than that between silicon and GaAs, it was still important to experimentally verify whether the substrate change would affect the blend morphology. Once it was confirmed that the presence of the  $\text{SiO}_2$  layer did not significantly alter the pattern characteristics (Figure 16), there was no need to repeat the full set of experiments conducted on silicon. The previously obtained data, on domain shapes, pseudo-periods, and fraction factors, could therefore be considered valid for the  $\text{SiO}_2$ -based process as well.

The main objective of this advanced process could then be addressed: to evaluate whether using a  $\text{SiO}_2$  sol-gel hard mask would allow for deeper etching into the silicon substrate. Unlike the PS mask alone, which limits the etch depth to approximately  $250\ \text{nm}$  due to its thickness, the  $\text{SiO}_2$  layer provides greater etch resistance and an unrestricted thickness, enabling the fabrication of gratings several hundred nanometers deeper. The results of this extended etching process are detailed in the following section.

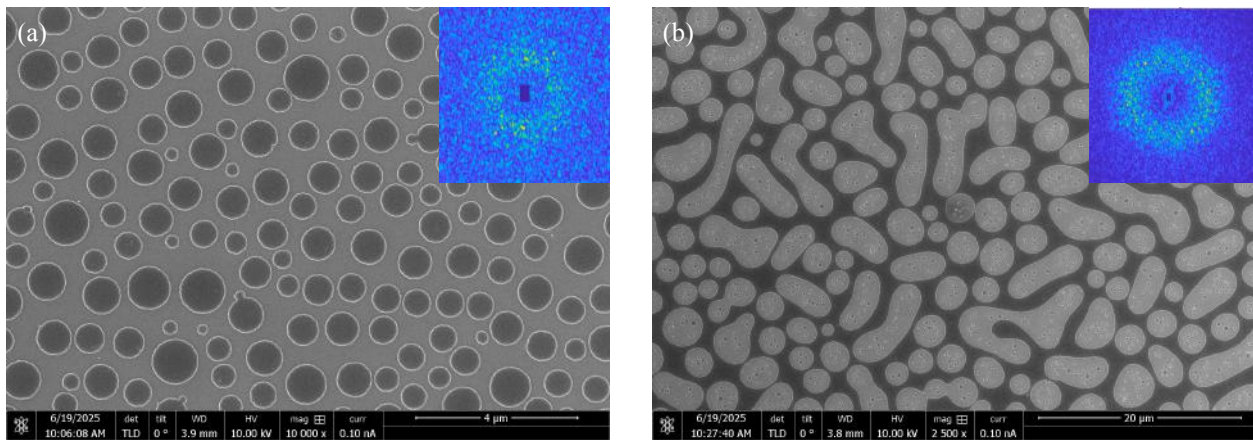


**Fig 16** : SEM images of the quasi-random patterns after etching  $\text{SiO}_2$ . The PB is spin-coated at 6K rpm, the polymer mass ratio PS/PMMA is 40/60 (a), 50/50 (b)



The results obtained using the advanced process confirm the effectiveness of this approach. By introducing a  $\text{SiO}_2$  layer as a hard mask on a silicon substrate beneath the polymer blend, I successfully preserved the morphology achieved by the polymer blend lithography, which remained consistent with what is typically observed on bare silicon. The  $\text{SiO}_2$  mask was well-defined and uniform, demonstrating that the pattern transfer from the polymer blend proceeds reliably onto the hard mask. While I was not able to etch the underlying silicon in this experiment due to the etching tool being temporarily unavailable, there are generally no issues or difficulties expected when etching silicon using a  $\text{SiO}_2$  mask. Overall, this process demonstrates a straightforward and robust strategy to increase grating depth while maintaining the self-assembled morphology of the polymer blend, confirming its potential for fabricating sub-micron quasi-random structures for light management in nanophotonic devices.

While the experimental results provided valuable insights into the influence of process parameters on the morphology of polymer blend patterns, they also raised several important questions regarding the underlying physical mechanisms governing the phase separation process. In particular, certain limitations and asymmetries observed experimentally, such as the failure to obtain usable structures at high PS concentrations (e.g., 70:30) or the imperfect morphological inversion between 60:40 and 40:60 compositions, highlight the need for a deeper theoretical understanding of the system. Although qualitative hypotheses can be made, for instance involving differences in viscosity, interfacial tension, or evaporation kinetics, these remain speculative without a more controlled framework in which to test them.

To address these open questions, I try developing a numerical model aimed at simulating the polymer blend phase separation process. The goal is to determine whether the experimentally observed limitations can be reproduced and explained within a physically consistent simulation. This includes exploring the asymmetry between PS-rich and PMMA-rich systems.

Beyond gaining insight into the fabrication process, this simulation framework also serves a longer-term purpose: it lays the groundwork for integrating realistic pseudo-periodic structures into optical simulations. By generating synthetic morphologies that closely resemble those obtained experimentally, we can eventually simulate light trapping and absorption ( $J_{\text{sc}}$ ) in ultra-thin solar cells that use polymer blend-based gratings.

### III / Polymer blend simulation

#### 1. Physics behind the Polymer blend model

To simulate the phase separation process observed in polymer blend lithography, we employ a diffusive model based on the Cahn–Hilliard equation, which is used to describe the mesoscale dynamics of phase separation in immiscible systems. This framework effectively captures the competition between interfacial energy, thermodynamic instability, and diffusion, which together drive the spontaneous self-organisation of the two polymers, PS and PMMA, into well-defined domains. At this stage, the system is modelled as a binary mixture, consisting only of PS and PMMA. The solvent, though central to the experimental process, is not explicitly included in the current formulation of the equation.

Nonetheless, some of the effects of solvent evaporation, particularly its influence on polymer mobility, are implicitly accounted for through parameter choices in the model, as detailed in the following sections. By doing so, we aim to retain a degree of realism in the simulation without introducing the full complexity of a ternary (polymer–polymer–solvent) system. This binary approach offers a first-level understanding of the blend’s behaviour, serving as a conceptual baseline. In subsequent stages, this model will be extended into a more comprehensive ternary framework by explicitly incorporating the solvent as an active component, enabling a more realistic description of the system’s dynamics.

Similarly to the treatment of the solvent, the influence of the substrate is not explicitly modelled in the current two-dimensional framework. Since the simulation is confined to a 2D plane parallel to the substrate, we do not resolve the vertical structure of the film nor include direct interactions at the polymer–substrate interface. However, the substrate’s effect is implicitly incorporated through the choice of parameters, such as mobility contrasts and interfacial energy coefficients. These values are adjusted to reflect the experimentally observed differences in polymer behaviour near the surface, including possible preferential wetting or immobilisation effects. While a full three-dimensional model would be required to capture substrate interactions more accurately, this effective approach allows us to reproduce key morphological trends observed in polymer blend lithography while maintaining computational efficiency.

In this model, the key variable is  $c(\vec{r}, t)$ , the local volume fraction of one of the polymers (PS in our case). This is an important distinction from the mass fraction used in the experimental section, where the PS:PMMA ratio was expressed in terms of the total mass of each polymer in solution. The conversion between the volume fraction and the mass fraction is straightforward but essential for consistency:

$$v = \frac{w \cdot \rho_{\text{PMMA}}}{w \cdot \rho_{\text{PMMA}} + (1 - w) \cdot \rho_{\text{PS}}} \quad (8)$$

where  $v$  is the volume fraction,  $\rho_i$  is the mass density of each polymer,  $w$  the mass fraction (ratio used in experiments). Since PS and PMMA have slightly different densities (around 1.05 g/cm<sup>3</sup> and 1.18 g/cm<sup>3</sup>, respectively), a 50:50 mass fraction does not correspond to an exactly symmetric volume fraction. This subtle imbalance can help explain why, in experiments, a nominally symmetric 50:50 mass ratio tends to produce a PS-rich matrix with dispersed PMMA domains, rather than a perfectly bicontinuous or symmetric structure between the two polymers.

To this end, we use the Cahn–Hilliard equation [16], a well-established framework for modelling phase separation in binary mixtures. The evolution of the local concentration field  $c(\vec{r}, t)$ , representing the local volume fraction of one polymer species (in our case PS), is governed by the generalised diffusion equation:

$$\frac{\partial c}{\partial t} = \nabla \cdot (D(c, t) \nabla \mu) \quad (9)$$

where:

- $D(c, t)$  is the composition and time dependent diffusion coefficient,
- $\mu$  is the chemical potential, defined as the variational derivative of the total free energy  $F[c]$ ,

and the boundary conditions are typically periodic in the in-plane directions.

The chemical potential is given by:

$$\mu = \frac{\delta F}{\delta c} = \frac{df}{dc} - \kappa \nabla^2 c$$

Here,  $\kappa$  is the gradient energy coefficient that penalises sharp concentration gradients, and  $f(c)$  is the local free energy density of the homogeneous mixture.

We model  $f(c)$  using the Flory–Huggins free energy density [17], which captures the entropic and enthalpic interactions between polymers A (PS) and B (PMMA):

$$f(c) = \frac{c}{N_A} \ln c + \frac{1-c}{N_B} \ln(1-c) + \chi c(1-c)$$

where:

- $N_A$  and  $N_B$  are the polymerisation degrees of PS and PMMA, respectively. (Number of monomer)
- and  $\chi$  is the Flory–Huggins interaction parameter, which determines the degree of immiscibility between the two polymers.

This free energy landscape typically exhibits a double-well shape, promoting phase separation into two distinct domains rich in either PS or PMMA. In the Flory-Hugging free energy density for a binary polymer blend, the volume fraction of polymer B (PMMA) is 1-c.

In the simplest case, the diffusion coefficient  $D$  is assumed to be constant, resulting in the classical form of the Cahn–Hilliard equation. Under this assumption, the equation can be efficiently solved in the Fourier domain, where the Laplacian operator becomes algebraic, allowing for fast and accurate evaluation of spatial derivatives using convolution properties. To ensure numerical stability while maintaining computational efficiency, I chose a semi-implicit time discretisation scheme. This approach avoids solving a fully nonlinear system at each time step, which would otherwise be required due to the logarithmic terms present in the Flory–Huggins free energy density when using a fully implicit method. That semi-implicit method give us the following equation :

$$\frac{\hat{c}^{n+1}(\mathbf{k}) - \hat{c}^n(\mathbf{k})}{\Delta t} = -D \left[ |\mathbf{k}|^2 \widehat{f'(c^n)} + \kappa |\mathbf{k}|^4 \hat{c}^{n+1}(\mathbf{k}) \right]$$

Conversely, a fully explicit scheme is not employed, as the fourth-order spatial derivative in  $c$  makes it highly numerical instabilities. This term strongly amplifies high-frequency noise, forcing the use of extremely small time steps to maintain stability. Such constraints render explicit integration impractical for simulations over realistic timescales.

In contrast to the constant-mobility case, the diffusion coefficient  $D$  in our model is explicitly dependent on space. This spatial dependence arises because  $D$  is a function of the local composition  $c(x, y)$ , since PS and PMMA have distinct intrinsic mobilities. The intrinsic mobility contrast between PS and PMMA arises partly from differences in chain rigidity and segmental friction [12]. The bulky phenyl side groups in PS increase chain stiffness, while the ester side groups in PMMA, introduce polarity that enhances inter-chain dipole–dipole interactions. This polarity increases segmental friction, reducing mobility compared to the more hydrophobic PS. The effective diffusion coefficient varies according to the local concentration of each polymer. In regions rich in PS, the mobility tends toward  $D_{PS}$ ; in PMMA-rich regions, it tends toward  $D_{PMMA}$ . Consequently, the diffusion coefficient cannot be factored out of the divergence operator, as is done in the constant-mobility formulation.

Moreover, even in the hypothetical case where  $D_{PS} = D_{PMMA}$ , the mobility is still not uniform throughout the domain. Experimental observations and physical reasoning both suggest that mobility is higher at PS–PMMA interfaces, where the environment is more disordered and less crowded, and lower in pure domains, where polymer chains are densely packed and more entangled. These effects motivate the use of a composition-dependent mobility function,  $D(c)$ , which introduces spatial variability into the system:  $D(c) \Rightarrow D(x, y)$ .

To capture both polymer-specific mobilities and the enhanced diffusion at interfaces, I chose to model the effective diffusion coefficient as:



$$D(c) = (D_{PS} \cdot c + D_{PMMA} \cdot (1 - c)) \cdot c(1 - c) \quad (10)$$

The first term,  $D_{PS} \cdot c + D_{PMMA} \cdot (1 - c)$ , represents a local average mobility weighted by the volume fractions of each polymer. This ensures that, in the limit of pure PS or pure PMMA, the mobility approaches the appropriate intrinsic value.

The second term,  $c(1 - c)$ , modulates the mobility to reflect enhanced diffusion at mixed interfaces and reduced diffusion in pure domains. It reaches a maximum when both polymers are present in equal proportions (i.e.,  $c = 0.5$ ) [17], and vanishes at  $c = 0$  or  $c = 1$ . This ensures that the highest mobility occurs at domain boundaries, consistent with physical intuition and prior experimental findings.

To account for the influence of the substrate in our 2D binary polymer blend model, I model an effective diffusion coefficient for each polymer species by averaging its position-dependent mobility across the film thickness. Specifically, the effective value of  $D_i$  (for  $i = PS, PMMA$ ) is calculated as:

$$D_i = \frac{1}{H} \int_0^H D_i(z) dz \quad (11)$$

where  $H$  is the total thickness of the polymer film (approximately 50 nm in our case). Since the exact vertical profile  $D_i(z)$  is not known analytically, I decided to approximate it using a piecewise constant model. I assume that the polymer has one diffusion coefficient  $D_{i,sub}$  near the substrate, up to a height  $z_0$ , and another coefficient  $D_{i,bulk}$  in the remaining upper part of the film. This leads to the following discrete approximation :

$$D_i = \frac{1}{H} \left( \int_0^{z_0} D_{i,sub} dz + \int_{z_0}^H D_{i,bulk} dz \right)$$

$$D_i = \frac{1}{H} (D_{i,sub} \cdot z_0 + D_{i,bulk} \cdot (H - z_0)) \quad (11)$$

This averaging enables us to incorporate vertical mobility gradients due to substrate interactions into our purely 2D simulation framework, capturing some of the influence of confinement and interfacial effects without explicitly modelling the vertical dimension.

To model the effect of solvent evaporation, we assume that the mobility of the polymers decreases progressively over time, reflecting the gradual loss of solubility and chain mobility as the solvent diminishes. This process leads to a form of kinetic arrest, where the system becomes frozen and diffusion slows down significantly.

We describe this behaviour by introducing a time-dependent decay of the diffusion coefficient for each polymer species [13]. The effective diffusion coefficient is modelled as:

$$D_i(t) = D_i \cdot e^{-\beta_i t} \quad (12)$$

where:

- $D_i$  represents the effective diffusion coefficient for each polymer species in solvent
- $\beta_i$  is a polymer-specific rate constant that controls how quickly polymer  $i$  loses its mobility during solvent evaporation.
- $t$  is the simulation time, corresponding to the drying timescale.

This exponential decay captures the progressive immobilisation of the polymers as the solvent evaporates. In early stages (small  $t$ ), diffusion is relatively high and phase separation can proceed. As  $t$  increases, mobility decreases rapidly, effectively freezing the system into its final morphology. This approach provides a simple yet effective way to account for drying dynamics without explicitly modelling the solvent concentration.

Since the solvent used, PGMEA, is polar, it exhibits greater affinity with PMMA, which is also polar, compared to PS, which is apolar. As a result, PMMA should remain soluble for a longer duration during the evaporation process, while PS loses its mobility more rapidly. This is reflected in our model by assigning a higher decay rate constant to PS:

$$\beta_{\text{PS}} > \beta_{\text{PMMA}}$$

indicating that the diffusion coefficient of PS decreases more quickly than that of PMMA as the solvent evaporates.

Taking all these effects into account, composition dependence, interfacial enhancement, substrate interface and temporal decay, we express the final form of the diffusion coefficient as:

$$D(c, t) = \left( D_{\text{ps}} \cdot e^{-\beta_{\text{ps}} t} \cdot c + D_{\text{pmma}} \cdot e^{-\beta_{\text{pmma}} t} \cdot (1 - c) \right) \cdot c(1 - c) \quad (13)$$

This formulation captures the combined influence of polymer-specific mobility, enhanced diffusion at interfaces, and solvent-driven time evolution, making it a physically grounded and spatially varying diffusion model for simulating polymer blend dynamics.

I added these complexities because the basic Cahn-Hilliard model alone was insufficient. Incorporating the Flory-Huggins potential lets us include the effect of molar mass in the system. Using a composition-dependent diffusion coefficient  $D$  explains the slight asymmetry observed with varying polymer ratios, while accounting for different solvent evaporation rates ( $\beta$ ) clarifies why phase separation fails at 70/30 but still works at 30/70.

However, introducing a composition-dependent diffusion coefficient  $D(c)$  significantly increases the complexity of the Cahn-Hilliard equation (the time dependence of  $D$  does not introduce extra complexity). In Fourier space, the presence of  $D(c)$  breaks the usual algebraic structure of the equation and introduces a convolution product, which arises from the fact that the product of two functions in real space becomes a convolution in Fourier space:

$$\frac{\hat{c}^{n+1}(\mathbf{k}) - \hat{c}^n(\mathbf{k})}{\Delta t} = -|\mathbf{k}|^2 \cdot D(\hat{c}^n, t) * \left[ \widehat{f'(c^n)} + \kappa |\mathbf{k}|^2 \hat{c}^{n+1}(\mathbf{k}) \right] \quad (14)$$

As before, we use a semi-implicit time integration scheme to preserve stability. To handle the added complexity from  $D(c)$ , I explored two approaches:

1. Fully nonlinear approach: keep the full convolution structure and solve the resulting nonlinear system using an iterative method such as Newton's method. While accurate (if we get the simulation to converge), this approach is computationally expensive and less suited for rapid simulations or parameter sweeps.
2. Approximate approach (chosen): to simplify the problem while retaining the essential physics, I apply an approximation. In the explicit term on the right-hand side, I treat  $D(c)$  as spatially uniform by replacing it with the spatial average of  $D$  at each time step:

$$D_{\text{mean}}^n(t) = \frac{1}{|\Omega|} \int_{\Omega} D(c^n, t) d\mathbf{r}$$

This leads to a simplified evolution equation in Fourier space:

$$\frac{\hat{c}^{n+1}(\mathbf{k}) - \hat{c}^n(\mathbf{k})}{\Delta t} = -|\mathbf{k}|^2 \cdot D(\hat{c}^n, t) \widehat{f'(c^n)} - \kappa D_{\text{mean}}^n(t) |\mathbf{k}|^4 \hat{c}^{n+1}(\mathbf{k}) \quad (15)$$

This approximation allows for a computationally efficient solution while still accounting for the average impact of composition-dependent mobility. Although it sacrifices the exact treatment of spatial coupling via convolution, it captures the main trends of phase separation and domain evolution, and provides a practical balance between realism and numerical tractability.

## 2. Comparison between simulation and experiments

For the simulation duration, I model the phase separation process over a total time of 8 seconds. Experimentally, I observed that after approximately 8 s, the colour no longer evolves significantly when spin-coating the polymers solution, indicating that the solvent has effectively evaporated and the polymers are kinetically trapped in their final configuration.

To reflect this behaviour in the simulation, the decay parameters  $\beta_{ps}$  and  $\beta_{pmma}$  are chosen such that the corresponding diffusion coefficients  $D_i(t)$  approach zero at  $t = 8$  s. This ensures that polymer mobility gradually decreases during the simulation and fully vanishes by the end, capturing the freezing effect caused by solvent loss.

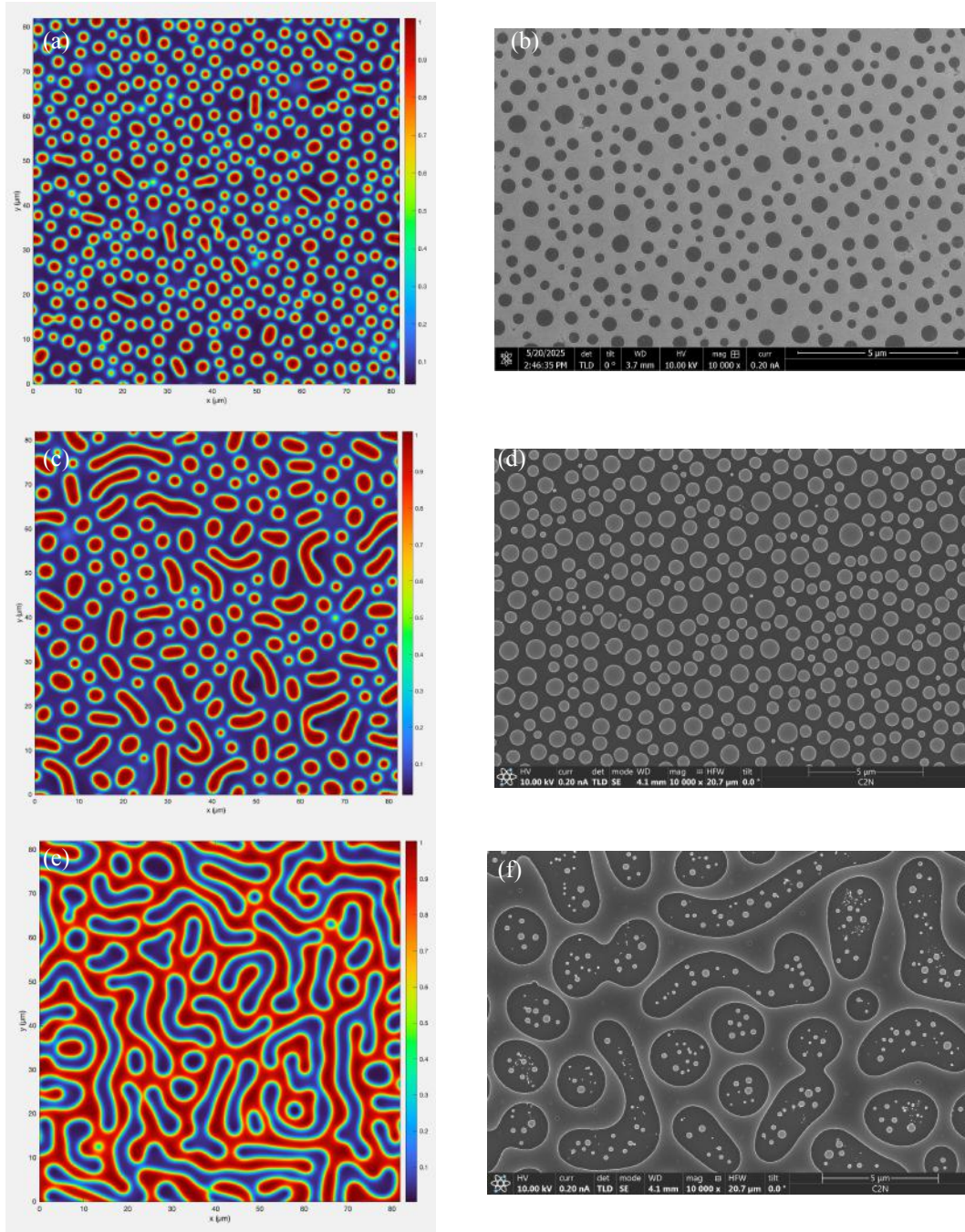


**Fig 17 :** The PB is spin-coated at 6K rpm, the polymer mass ratio PS/PMMA is 30/70 (a) and (b) , 40/60 (c) and (d) , 50/50 (e) and (f). (a),(c),(e) is from simulation and (b), (d), (f) is from experiments



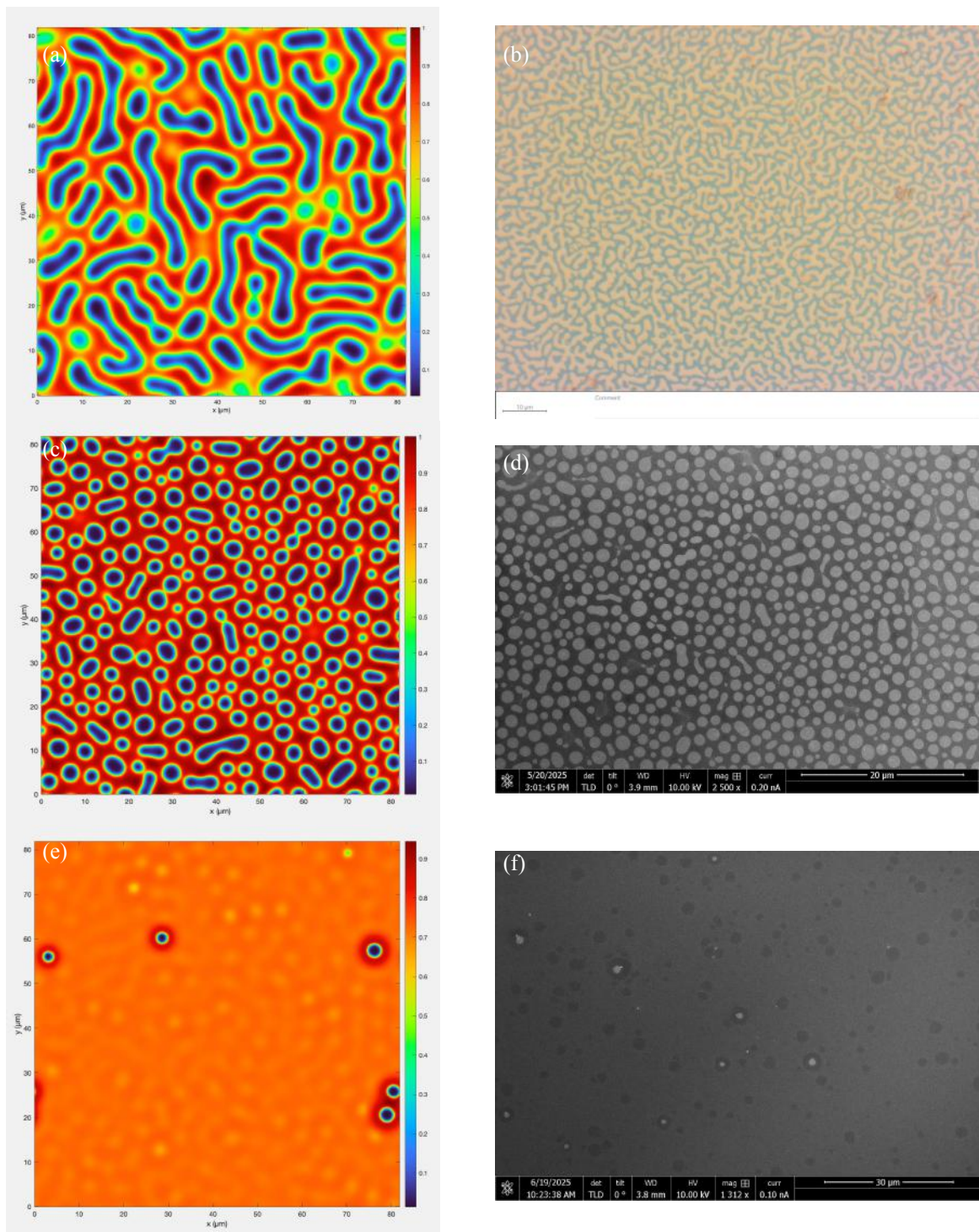


**Fig 18:** The PB is spin-coated at 6K rpm, the polymer mass ratio PS/PMMA is 50/50 (a) and (b) , 60/40 (c) and (d) , 70/30 (e) and (f). (a),(c),(e) is from simulation and (b), (d), (f) is from experiments. The molar mass of PMMA is 950 kg/mol, the molar mass of PS is 100 kg/mol in (a) and (b)

In the simulation images (shown on the left Figures 18 and 19), the colour bar represents the local volume fraction  $c$ , where  $c = 1$  corresponds to regions composed purely of PS, and  $c = 0$  corresponds to regions composed purely of PMMA. Overall, the simulation captures many key features observed experimentally. The general morphology, domain distribution and pattern inversion aligns well with what we see in the lab.

Notably, the simulation successfully reproduces the inversion of the pattern between PS-dominant and PMMA-dominant compositions, a key feature also observed in the experimental results. It also captures the failure of phase separation when the initial mass fraction of PS reaches 70%, which corresponds to the experimental observation that no well-defined PMMA domains are formed at this composition.

The simulation provides valuable insight into the origin of this limitation. It suggests that the asymmetry arises from the different affinities between the solvent (PGMEA) and the two polymers. Specifically, since PMMA remains soluble for a longer time due to its better compatibility with the polar solvent, it continues to diffuse even as PS begins to solidify. When the PS content exceeds 70%, PS rapidly becomes immobile and cannot form distinct domains, leading instead to a nearly homogeneous film dominated by PS. This could explain why no phase-separated structures are observed experimentally for high PS fractions.

However, some differences remain. For example, when the PS mass fraction is less than or equal to 50%, the simulated domains tend to be less circular than those in the experiments, suggesting that interfacial effects or anisotropies may not be fully captured. Additionally, the scale of the simulated features is generally larger than in the experimental results; the blobs are often too big, even if their overall shape and distribution resemble what we observe in practice.

Despite these limitations, the simulation successfully reproduces the qualitative behaviour of the system and offers valuable insight into the mechanisms behind the pattern formation seen in polymer blend lithography.

## IV/ Conclusion

In this chapter, we explored polymer blend lithography as a low-cost, simple method to create pseudo-periodic nano-structures. By combining experimental work and numerical simulations, we developed a deeper understanding of how the process works and how we can tune the resulting patterns.

Through a systematic study of polymer ratios and spin-coating speeds, we demonstrated that we could control the size and morphology of the domains formed by phase separation. By analysing key parameters such as the pseudo-period, surface coverage, and circularity, we were able to link processing conditions to the final structure. We showed, for example, that increasing the spin speed shrinks the pattern, and that moving from a PS dominant to PMMA dominant inverts the pattern, though not perfectly, due to asymmetries in polymer behaviour.

This control was made possible by building a physical understanding of the mechanisms behind polymer blend phase separation. Using a binary Cahn–Hilliard model as a foundation, we simulated how PS and PMMA self-organise during solvent evaporation. By trying to include more physical elements such as composition-dependent diffusion, interface-enhanced mobility, and time-dependent freezing of the polymers, we were able to reproduce many of the experimental observations.

Thanks to this combined approach, we achieved a level of predictability and reproducibility in the fabrication process. Even more importantly, we now have the ability to tune the feature size of the grating by adjusting parameters like the spin speed, polymer ratio, or etch duration, making this technique more versatile for applications in photovoltaics.

The simulation results also suggest that using polymers with lower molar mass could lead to smaller domain sizes, offering a promising route to reduce dimensions in the final pattern. In addition, our model suggests that using polymers with lower molar mass could potentially allow us to move further away from equilibrium in terms of mass fraction such as reaching stable phase separation even at 70:30 compositions. This could help overcome the limitations we observed experimentally for high PS concentrations, where domain formation typically fails. These insights will soon be tested experimentally to validate the impact of molar mass on pattern morphology. On the simulation side, our next step is to try to find a more suitable set of constants ( $D$ ,  $\kappa$ ,  $\chi$ ) to improve the quantitative accuracy of the model. To achieve this, we plan to implement surrogate optimization that compares simulation outputs with experimental data and adjusts the parameters to achieve the best possible fit.

## Chapter 4 : Silicon Thinning

### I / Introduction

The goal of this chapter is to investigate practical methods for thinning silicon wafers in a controlled, reproducible, and cost-effective way. In the context of our project, ultra-thin silicon solar cells, reducing the thickness of the active silicon layer plays a key role in minimising fabrication costs. However, commercial ultra-thin silicon wafers, typically in the 10 to 40  $\mu\text{m}$  range, remain expensive and fragile, making them unsuitable for exploratory research or scalable prototyping. As a result, we aim to develop an in-house thinning process starting from commercially available silicon wafers.

Throughout this chapter, we explore an approach for thinning silicon wafers with wet etching [6]. The challenge is to find a balance between thinning efficiency and surface integrity, so that the resulting wafer can be processed further for integration into a complete solar cell.

In addition to the technical challenges, reproducibility and scalability are essential considerations. The process should be robust enough to be repeated reliably across multiple samples. At the same time, we aim to avoid high-cost equipment or hazardous chemicals whenever possible, in line with the broader goal of low-cost solar energy technologies.

In summary, this chapter lays the groundwork for fabricating high-performance, ultra-thin silicon solar cells by addressing one of the key bottlenecks: the production of ultra-thin, clean, and usable silicon substrates from standard wafers. Our focus is not only on achieving the desired target thickness but also on ensuring that the surface roughness remains compatible with subsequent light-trapping layers and device fabrication. Determining the etching rate is also necessary to calculate the etching duration needed to achieve the desired thickness, given the initial layer thickness.

### II / Silicon thinning process

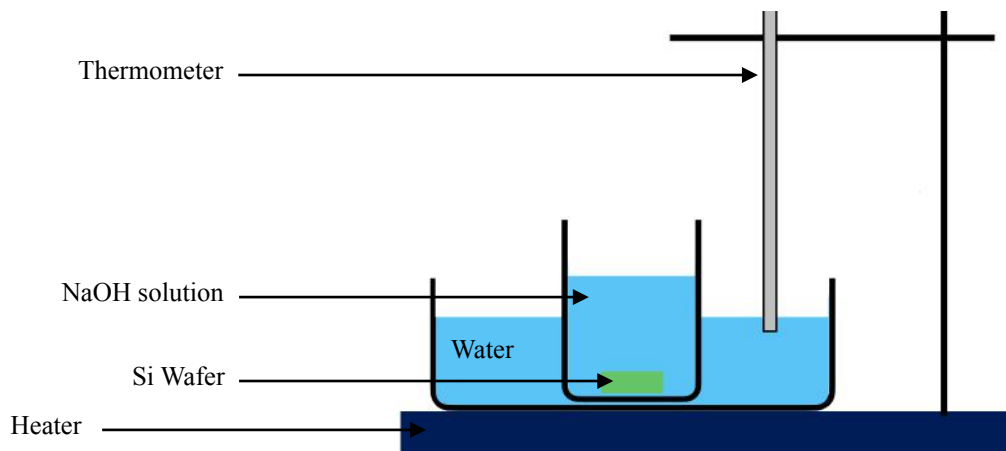


Fig 19: Layout for the silicon thinning process

For this study, we used a 400  $\mu\text{m}$ -thick silicon wafer coated with a 100 nm thermal  $\text{SiO}_2$  layer on the top surface, and a multilayer stack of  $\text{SiO}_2/\text{Ti}/\text{Ag}/\text{Ti}/\text{Au}$  on the back surface.

Before etching, the silicon sample is prepared by bonding it onto a borosilicate glass substrate using LOCTITE Eccobond 931 (epoxy). This setup exposes only one face of the wafer to the etchant and provides mechanical stability throughout the process. This is especially important since the final silicon thickness is reduced to just 10 - 40  $\mu\text{m}$ , a level at which the wafer becomes extremely fragile and difficult to handle without support. To further ensure uniformity during etching, the sample is positioned flat at the bottom of the glass container in a horizontal orientation. This placement prevents gas bubbles, produced by the highly effervescent reaction with NaOH, from remaining on the surface, which could otherwise lead to localised roughness or uneven thinning.



Another crucial step before immersion, it is essential to remove the thermal silicon dioxide ( $\text{SiO}_2$ ) layer using  $\text{SF}_6$  RIE. In the subsequent wet etching solution at 70 °C, silicon etches roughly 600 times faster than  $\text{SiO}_2$  [14]. If any thermal oxide remains on the surface, the etching front will not reach the Si/ $\text{SiO}_2$  interface simultaneously across the sample. Regions where the oxide is absent will start etching silicon much earlier, while areas still covered by oxide will lag behind. This mismatch leads to severe surface roughness and step formation, ultimately degrading the functional quality of the etched surface. Complete oxide removal prior to immersion ensures a synchronized start of silicon etching across the entire wafer.

In this study, silicon thinning is achieved through a controlled wet etching process, selected for its simplicity and low cost process [6]. The etchant is a solution composed of 20 g of sodium hydroxide ( $\text{NaOH}$ ) in 50 mL of deionised water [6]. This solution is heated to 70 °C in a bain-marie to ensure uniform and stable temperature throughout the liquid, a key factor in maintaining a consistent etch rate. The temperature is regulated using a setup that couples a heater and a thermometer, allowing reliable thermal regulation without requiring mechanical agitation, which could disturb the process.

While  $\text{NaOH}$  hot and concentrated is known to slowly etch glassware and potentially release fine glass particles into the solution, we chose borosilicate glass containers for their superior thermal conductivity compared to Teflon. This decision ensured more efficient and homogeneous heating, and no contamination from glass particles was observed on the etched surfaces, confirming the suitability of this choice under our conditions.

### III / Experimental results

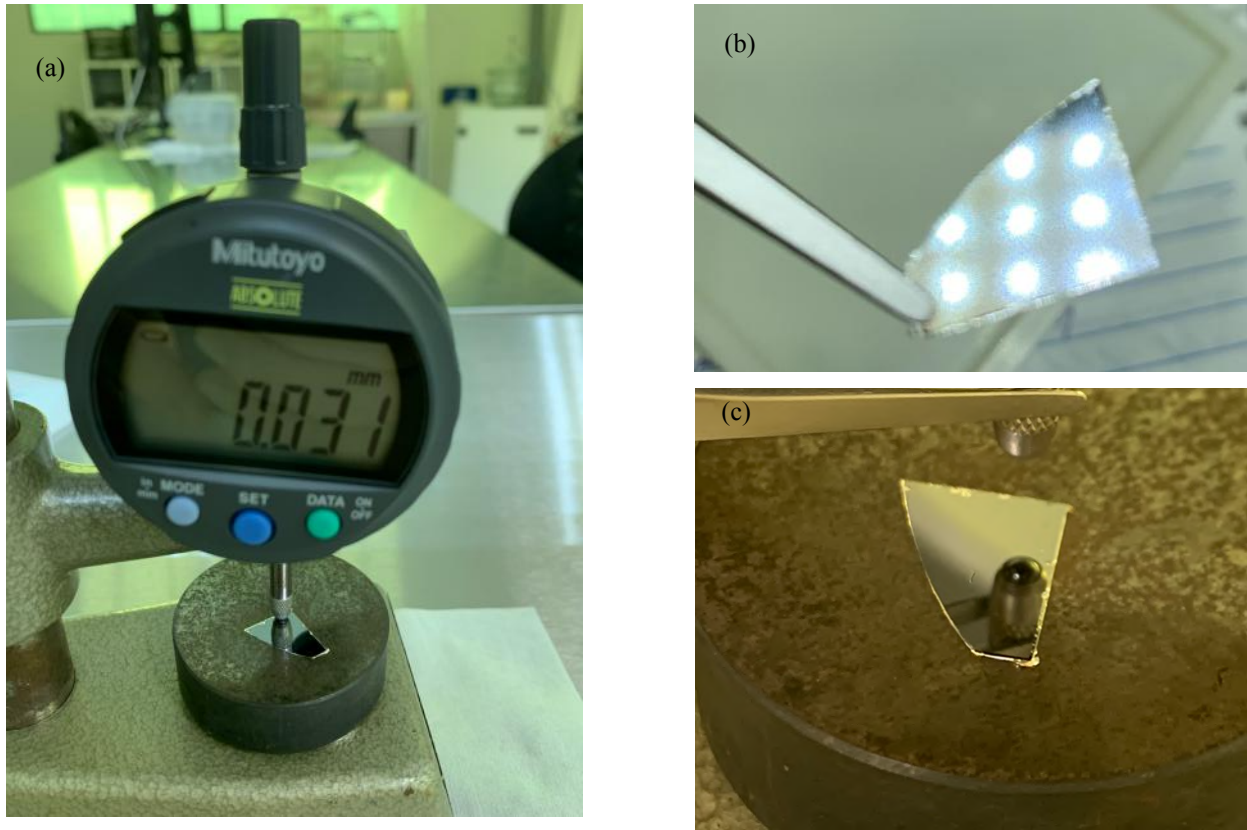


**Fig 20** : Etched sample after 4h in the  $\text{NaOH}$  solution and 5 minutes water rinse

After the etching process, the sample was rinsed for 5 minutes in deionised water, and its appearance is shown in Figures 21b and 21c. A visual inspection suggested that the surface was generally smooth: in Figure 21c it appears mirror-like, while in Figure 21b, illumination reveals scattered reflections, indicating slight surface roughness. This roughness can also be observed under an optical microscope (Figure 22d). profilometer measurements show height variations of approximately 100–400 nm over widths of several tens of micrometres. Such roughness is likely caused by local variations in the etching rate.

During etching, we observed partial delamination of the sample from the glass substrate, as the Eccobond adhesive lost adhesion. This poses a challenge for process repeatability and reliability. Three potential solutions were considered:

1. Remove the glass substrate during etching and glue the silicon to glass after thinning. However, once thinned to 10–40  $\mu\text{m}$ , the wafers are too fragile to handle safely.
2. Lower the etching temperature to reduce heat-induced adhesive degradation. This would, however, slow the etch rate and reduce throughput.
3. Modify the glass surface (e.g., plasma activation) to improve bonding with Eccobond and maintain adhesion throughout the process.

From multiple experiments, we measured an average etching rate of  $\sim 90\text{--}95\text{ }\mu\text{m/h}$  under standard conditions. Thicknesses were measured using an electronic gauge. For example, after 4 hours of etching, the wafer reached 30  $\mu\text{m}$  (Figure 21a), consistent with the estimated rate.

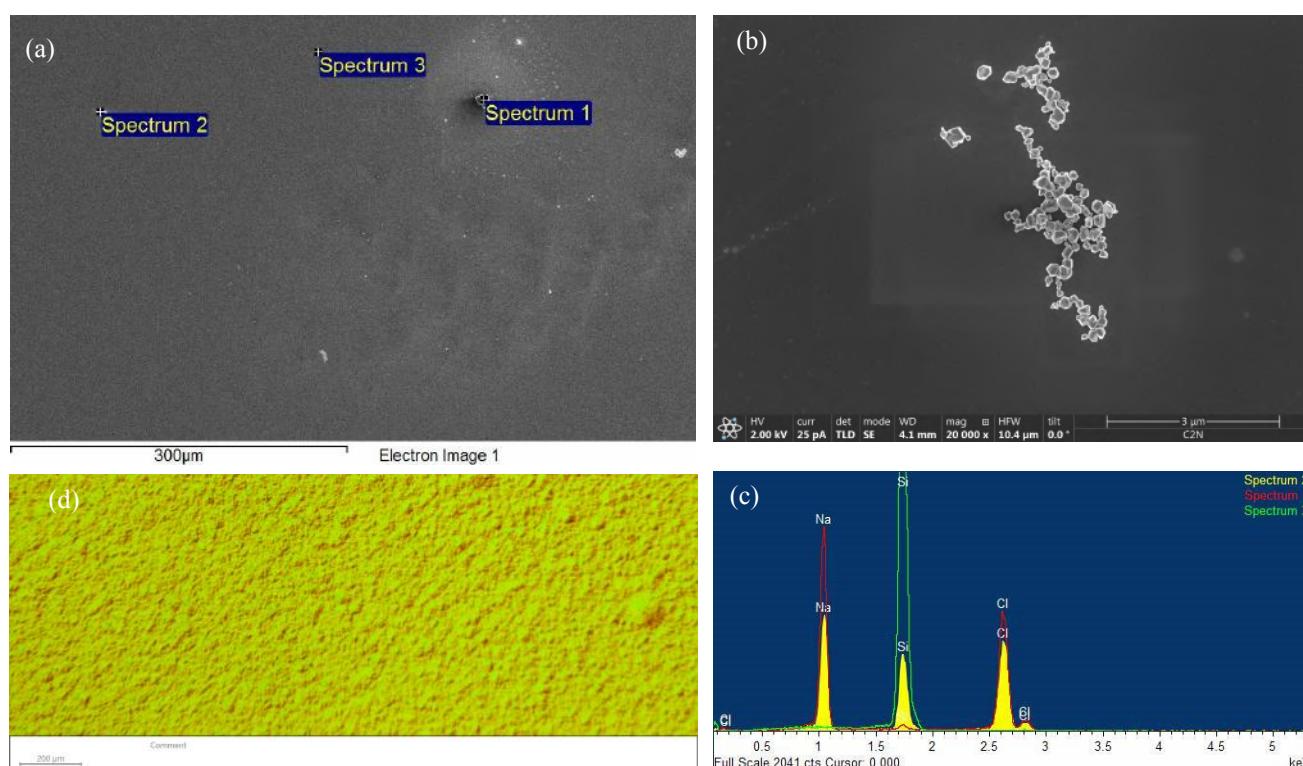


**Fig 21 :** Energy-dispersive X-ray spectroscopy (EDX) analysis of the silicon surface after 2 h 30 min of etching, followed by a brief rinse in deionised water and a 3-minute treatment in HCl. (a) Overview of the etched silicon surface; (b) Close-up of a defect area analysed at Spectrum 2; (c) EDX spectra recorded at different locations across the sample. (d) Optical microscope image of the surface.

Initially, no post-etch water rinse was performed, and scanning electron microscopy (SEM) revealed crystalline residues on the surface (Figure 22b). To remove these, we applied a 3-minute HCl bath, which eliminated many of the defects. However, some visible deposits remained and were identified by EDX analysis as sodium chloride (NaCl): Spectra 1 and 2 from these areas showed sodium and chlorine, while Spectrum 3 from a clean area showed only silicon (Figure 22c). The NaCl formation was likely due to the reaction between HCl and sodium-containing residues.

To avoid NaCl formation, we replaced the HCl step with a 5-minute rinse in deionised water immediately after etching. This proved very effective at removing the sodium-containing residues.

Another type of contamination observed on the surface consisted of Fe- and Ni-containing defects. We were able to eliminate this contamination by handling the sample with Teflon tweezers instead of using a stainless steel tweezers while the tweezers were in contact with the solution.

## IV / Conclusion

In this chapter, we detailed the development and optimisation of a wet etching process for silicon thinning, aiming to achieve thin, clean, and defect-free silicon layers. Using a NaOH-based solution heated to 70 °C, we successfully reduced the thickness of 400 µm silicon wafers to the target range of 10-40 µm. We managed to determine the average etch rate equal to 90-95 µm per hour.

Surface inspection revealed mirror-like finishes with minor roughness and occasional crystalline residues. SEM and EDX analyses confirmed the presence of crystals on the surface after etching, but a longer rinse in deionised water and the use of a Teflon tweezers proved being efficient, eliminating most of the remaining crystals.

Adhesion issues between the silicon sample and the Eccobond, caused by temperature-induced degradation of the Ecobond adhesive, were also identified. Several strategies were proposed to mitigate this, including lowering the process temperature, improving substrate surface preparation, or modifying the bonding method.

Overall, the developed process provides a viable approach to producing ultra-thin silicon wafers with good surface quality. The surface finish appears sufficiently good to consider integrating this process into our complete ultra-thin silicon solar cell with light-trapping structures. However, further improvements in surface quality are still being explored, such as adding hydroxyl amine to the etching solution [6] or adjusting its concentration and temperature.

## General Conclusion

This report presents a comprehensive exploration of innovative strategies to advance ultra-thin tandem solar cell technologies, from optical design and nano-patterning to substrate engineering. Each chapter contributes a critical piece to the global goal of developing high-performance, lightweight, and cost-effective photovoltaic devices.

In the second chapter, we focused on optical simulations to design ultra-thin tandem cells composed of an  $\text{Al}_{0.25}\text{GaAs}$  top cell and a silicon bottom cell. By implementing advanced light-trapping structures, such as periodic gratings and Bragg mirrors, we demonstrated that it is possible to significantly reduce absorber thicknesses while preserving current matching and high short-circuit current densities ( $J_{\text{sc}}$ ). Our results highlighted the need to carefully balance spectral filtering and light confinement, showing that different optical strategies may be better suited depending on the application: Bragg mirrors for compact, lightweight systems and dual-grating designs for maximal efficiency.

In the third chapter, we turned to the experimental and theoretical investigation of polymer blend lithography as a scalable and low-cost method for producing pseudo-periodic nano-structures. By combining polymer blend experiments with phase-field simulations based on the Cahn–Hilliard model, we gained insights into the mechanisms governing domain formation and morphology. This allowed us to develop predictive control over the pattern features, such as shape and distribution, opening a path toward tailored nano-patterns for solar cell light trapping. Additionally, our results suggest promising avenues for further miniaturising these features by using lower molar mass polymers. Fitting our current model to experimental data to optimize the physical parameters also appears to be a valuable approach to making the simulation more quantitative.

The fourth chapter addressed the practical challenge of thinning silicon wafers to the tens-of-microns scale using a wet etching process. We achieved reproducible thinning of 400  $\mu\text{m}$  silicon down to as little as 30  $\mu\text{m}$  with good surface quality and minimal roughness. Although we observed some challenges, such as surface crystallite formation and adhesion loss due to Ecobond degradation, we proposed and tested viable alternative strategies. These efforts are crucial for integrating high-quality ultra-thin silicon into complete tandem solar cell structures.

Altogether, this work demonstrates a multidisciplinary effort combining optical simulation, materials science, experimental fabrication, and numerical modeling to address the key bottlenecks in developing next-generation ultra-thin tandem solar cells. The methods and results presented in this report contribute to both the fundamental understanding and the practical advancement of ultra-thin photovoltaic technologies, with strong potential for applications in flexible, lightweight, and high-efficiency solar energy systems.

## Appendix

Values for the polymer blend simulation (figures 17 and 18) are :

- $dt = 1e-3$  time step (s)
- $\chi = 0.086$  interaction parameter
- $N_{PS} = 960$  polymerisation of PS (number of monomer per chain)
- $N_{PMMA} = 1000$  polymerisation of PMMA (number of monomer per chain)
- $d_{PMMA} = 1.18$  density of PMMA ( $g \cdot cm^{-3}$ )
- $d_{PS} = 1.05$  density of PS ( $g \cdot cm^{-3}$ )
- $a_{PS} = 1.8e-9$  monomer size of PS (nm)
- $a_{PMMA} = 1.7e-9$  monomer size of PMMA (nm)
- $D_{PS}^{bulk} = 1e-9$  mobility of PS far from the interface with the substrate ( $m^2 \cdot s^{-1}$ )
- $D_{PMMA}^{bulk} = 5e-10$  mobility of PMMA far from the interface with the substrate ( $m^2 \cdot s^{-1}$ )
- $D_{PS}^{Sub} = 1e-11$  mobility of PS close from the interface with the substrate ( $m^2 \cdot s^{-1}$ )
- $D_{PMMA}^{Sub} = 5e-13$  mobility of PMMA close from the interface with the substrate ( $m^2 \cdot s^{-1}$ )
- $\beta_{PS} = 1$  evaporation rate constant of PS ( $s^{-1}$ )
- $\beta_{PMMA} = 0.2$  evaporation rate constant of PMMA ( $s^{-1}$ )
- $z_0 = 10$  nm distance from the substrate where I consider that polymers are not at the interface anymore



## References

- [1] Phuong-Linh Nguyen. Gluing III-V//Si with transparent conductive layers for tandem solar cells. Micro and nanotechnologies/Microelectronics. Université Paris-Saclay, 2022. English. NNT : 2022UP-AST069.
- [2] Buencuerpo. Jeronimo, et al. Nano Energy, vol. 96, 2022, article 107080.
- [3] Cahn, John W.; Hilliard, John E. (1958). "Free Energy of a Nonuniform System. I. Interfacial Free Energy". *The Journal of Chemical Physics*. **28** (2). AIP Publishing: 258–267.
- [4] Chen, HL., Cattoni, A., De Lépinau, R. *et al.* A 19.9%-efficient ultrathin solar cell based on a 205-nm-thick GaAs absorber and a silver nanostructured back mirror. *Nat Energy* **4**, 761–767 (2019). <https://doi.org/10.1038/s41560-019-0434-y>.
- [5] Inès Massiot, Andrea Cattoni, Stéphane Collin. Progress and prospects for ultrathin solar cells. *Nature Energy*, 2020, 5, pp.959-972. 10.1038/s41560-020-00714-4. Hal-02999759.
- [6] Swarnalatha, V., Purohit, S., Pal, P. *et al.* Enhanced etching characteristics of Si{100} in NaOH-based two-component solution. *Micro and Nano Syst Lett* **10**, 10 (2022). <https://doi.org/10.1186/s40486-022-00152-9>
- [7] F. Vermolen, P. L. J. Zitha. Numerical Solutions of Some Diffuse Interface Problems: The Cahn-Hilliard Equation and the Model of Thomas and Windle. *International Journal for Multiscale Computational Engineering*
- [8] Franck Boyer, Céline Lapuerta. Study of a three component Cahn-Hilliard flow model. Vol. 40, N°4, 2006, pp. 653–687
- [9] K. Biswas, S. Kal. Etch characteristics of KOH, TMAH and dual doped TMAH for bulk micromachining of silicon. [www.elsevier.com/locate/mejo](http://www.elsevier.com/locate/mejo)
- [10] Vladimir F. Kleptsyn and Johannes G. Smits. Temperature Dependent Etching of (100) and (110) Silicon in NaOH and in Tetramethyl-Ammonium Hydroxide, College of Engineering, Boston University.
- [11] Cahn, John W.; Hilliard, John E. (1958). "Free Energy of a Nonuniform System. I. Interfacial Free Energy". *The Journal of Chemical Physics*. **28** (2). AIP Publishing: 258–267
- [12] Chemistry Division, Naval Research Laboratory, Washington, DC, 20375-5342, USA.
- [13] F. Tanaka, T. Araki, et al., "Polymer blend phase separation induced by solvent evaporation," *Journal of Chemical Physics*, 1996, 104(14), 5734-5740.
- [14] Wet-chemical etching of silicon and SiO<sub>2</sub>, MicroChemicals GmbH
- [15] M. G. Moharam and T. K. Gaylord. Rigorous coupled-wave analysis of planar-grating diffraction. *J. Opt. Soc. Am.*, 71(7):811–818, 1981.
- [16] Cahn, John W.; Hilliard, John E. (February 1958). "Free Energy of a Nonuniform System. I. Interfacial Free Energy". *The Journal of Chemical Physics*. **28** (2): 258–267. Bibcode:1958JChPh..28..258C. doi:10.1063/1.1744102.
- [17] Berry, J; et al. (2018). "Physical principles of intracellular organization via active and passive phase transitions". *Reports on Progress in Physics*. **81** (46601): 046601. Bibcode:2018RPPh...81d6601B. doi:10.1088/1361-6633/aaa61e.



## Abstract

The development of ultra-thin solar cells is driven by the need for lightweight, flexible, and resource-efficient photovoltaic technologies. Thinning down solar absorbers reduces material usage and manufacturing costs, while also enabling applications in portable devices, flexible substrates, and space-constrained environments. However, this reduction in thickness presents a fundamental challenge: maintaining high optical absorption with less material. This work explores several light-trapping strategies to address this issue through a combination of optical simulations, nano-fabrication techniques, and process optimisation.

Using Rigorous Coupled-Wave Analysis (RCWA), we investigated periodic nano-structures such as diffraction gratings and Bragg mirrors to enhance absorption and improve current matching in tandem solar cells. Two configurations were compared: a dual-grating system and a hybrid Bragg mirror–grating structure. The study revealed trade-offs between total photocurrent and spectral selectivity, with each design being more suitable depending on the absorber thickness and target application.

To go beyond ideal periodic designs, we explored polymer blend lithography as a scalable, bottom-up approach to create pseudo-periodic nano-structures. By tuning polymer ratios and spin-coating parameters, we demonstrated control over the resulting patterns. These experimental results were supported by simulations using a composition-dependent phase-field model, providing insights into phase separation dynamics and structure formation. This approach offers a promising route to fabricate disordered light-trapping layers with controlled optical response, even in the absence of perfect periodicity.

Finally, to physically realise ultra-thin silicon solar cells, we are developing a wet etching process capable of reducing standard 400  $\mu\text{m}$  wafers to thicknesses below 40  $\mu\text{m}$  with clean surfaces. The process is monitored and optimised to ensure reproducibility and compatibility with downstream integration steps.

Together, these three components lay the foundation for next-generation lightweight photovoltaic devices, combining advanced optical design, bottom-up nano-fabrication, and materials engineering.

## Résumé

Le développement de cellules solaires ultra-minces est motivé par le besoin croissant de technologies photovoltaïques légères, flexibles et économes en ressources. Réduire l'épaisseur des couches absorbantes permet de diminuer la consommation de matériau et les coûts de fabrication, tout en ouvrant la voie à des applications sur dispositifs portables, substrats flexibles ou environnements contraints comme l'espace. Cependant, cette réduction d'épaisseur pose un défi fondamental : maintenir une absorption optique élevée avec moins de matière. Ce rapport explore plusieurs stratégies de piégeage optiques pour répondre à cette problématique, en combinant simulations optiques, techniques de nano-fabrication et optimisation des procédés.

À l'aide de la méthode Rigorous Coupled-Wave Analysis (RCWA), nous avons étudié des nano-structures périodiques telles que des réseaux de diffraction et des miroirs de Bragg afin d'augmenter l'absorption et d'améliorer l'équilibrage du courant dans des cellules solaires tandem. Deux configurations ont été comparées: un système à double réseau et une structure hybride combinant miroir de Bragg et réseau. L'étude a mis en évidence des compromis entre photocourant total et sélectivité spectrale, chaque design étant plus ou moins adapté selon l'épaisseur des couches absorbantes et l'application visée.

Pour dépasser les limites des structures strictement périodiques, nous avons exploré la lithographie par mélange de polymères permettant de créer des nano-structures pseudo-périodiques. En ajustant les ratios de polymères et les paramètres de spin-coating, nous avons démontré la capacité à contrôler la morphologie des motifs formés. Ces résultats expérimentaux ont été soutenus par des simulations utilisant un modèle de champ de phase dépendant de la composition, offrant un aperçu des dynamiques de séparation de phase et de la formation des structures. Cette approche ouvre la voie à la fabrication de couches de piégeage de lumière désordonnées mais aux réponses optiques maîtrisées, même en l'absence de périodicité parfaite.

Enfin, afin de concrétiser la fabrication de cellules solaires ultra-minces à base de silicium, nous développons un procédé de gravure humide capable de réduire des wafers standards de 400  $\mu\text{m}$  d'épaisseur à des valeurs inférieures à 40  $\mu\text{m}$ , tout en maintenant des surfaces propres et lisses. Ce procédé est optimisé pour garantir sa reproductibilité et sa compatibilité avec les étapes d'intégration ultérieures.

Ensemble, ces trois volets constituent les bases des dispositifs photovoltaïques de nouvelle génération, alliant conception optique avancée, nano-fabrication et ingénierie des matériaux.

## Riassunto

Lo sviluppo di celle solari ultra-sottili è motivato dalla crescente necessità di tecnologie fotovoltaiche leggere, flessibili ed efficienti dal punto di vista delle risorse. Ridurre lo spessore degli strati assorbenti consente di diminuire il consumo di materiali e i costi di produzione, aprendo al contempo la strada ad applicazioni in dispositivi portatili, substrati flessibili o ambienti con vincoli di spazio come lo spazio. Tuttavia, questa riduzione di spessore pone una sfida fondamentale: mantenere un'elevata assorbimento ottico con meno materiale. Questo rapporto esplora diverse strategie di intrappolamento della luce per affrontare questa problematica, combinando simulazioni ottiche, tecniche di nano-fabbricazione e ottimizzazione dei processi.

Utilizzando il metodo Rigorous Coupled-Wave Analysis (RCWA), abbiamo studiato nano-strutture periodiche come reticoli di diffrazione e specchi di Bragg per aumentare l'assorbimento e migliorare il bilanciamento della corrente in celle solari tandem. Sono state confrontate due configurazioni: un sistema con doppio reticolo e una struttura ibrida che combina uno specchio di Bragg con un reticolo. Lo studio ha evidenziato compromessi tra foto-corrente totale e selettività spettrale, con ciascun design più o meno adatto in base allo spessore degli assorbitori e all'applicazione prevista.

Per superare i limiti delle strutture rigorosamente periodiche, abbiamo esplorato la litografia a miscela di polimeri, che consente di creare nano-strutture pseudo-periodiche. Regolando i rapporti tra i polimeri e i parametri di spin-coating, abbiamo dimostrato la possibilità di controllare la morfologia dei pattern formati. Questi risultati sperimentali sono stati supportati da simulazioni che utilizzano un modello di campo di fase dipendente dalla composizione, offrendo una comprensione della dinamica della separazione di fase e della formazione delle strutture. Questo approccio apre la strada alla realizzazione di strati disordinati per l'intrappolamento della luce, ma con risposte ottiche controllate, anche in assenza di perfetta periodicità.

Infine, per rendere concreta la realizzazione di celle solari ultra-sottili in silicio, stiamo sviluppando un processo di incisione chimica umida capace di ridurre i wafer standard da 400  $\mu\text{m}$  a spessori inferiori a 40  $\mu\text{m}$ , mantenendo superfici pulite e lisce. Il processo è ottimizzato per garantirne la riproducibilità e la compatibilità con le successive fasi di integrazione.

Nel complesso, questi tre approcci costituiscono le fondamenta dei dispositivi fotovoltaici di nuova generazione, combinando progettazione ottica avanzata, nano-fabbricazione e ingegneria dei materiali.

## Presentation of the company

The Centre for Nanosciences and Nanotechnologies (C2N) is a premier joint research unit (UMR 9001) operated by CNRS and Université Paris-Saclay, located at the heart of the Paris-Saclay campus in Palaiseau, France. Established by merging the Institute for Fundamental Electronics and the Laboratory for Photonics and Nanostructures, C2N has been fully operational since 2017 and now stands among the largest nanoscience laboratories in the Paris region .

C2N's research spans a wide range of disciplines, such as materials science, nanophotonics, nanoelectronics, microsystems, and nanobiotechnology. It operates one of France's most advanced cleanrooms, equipped for micro- and nanofabrication, epitaxy, and advanced material characterization. This facility is open to both academic and industrial collaborators and is integrated into France's national micro-nano technology network .

Among its key divisions is the Photonics Department, which bridges fundamental research and device innovation. It focuses on hybrid integration, micro- and nano-photonics, and the development of optical systems across visible to infrared wavelengths. This is in this department that I worked in, and more specifically in the ODIN Team.

Within C2N's Photonics Department, the ODIN team (Optoelectronic Devices and INnovation) brings together multiple research groups collaborating closely on semiconductor-based optoelectronic devices that span the UV to THz range .

Key areas of activity include:

- Mid-IR and THz devices, such as quantum cascade lasers and detectors.
- Integrated light sources, including III-V semiconductors and flexible components.
- Nanowire-based photovoltaic applications, aligning with next-generation solar energy technologies.
- Nano-structured flexible LEDs and piezoelectric sensors.

The team integrates both experimental fabrication capabilities and applied innovation by leveraging C2N's cleanroom infrastructure .

A highlight within ODIN is the SUNLIT team, launched in 2014 by Stéphane Collin and Andrea Cattoni. This group specializes in light-trapping strategies for ultra-thin solar cells, exploring how nanostructuring can dramatically enhance absorption while reducing material use. Under their leadership, the team achieved significant breakthroughs, demonstrating record efficiencies with solar cells as thin as a few hundred nanometers and developing foundational technology for photovoltaic miniaturization .

## Internship summary sheet

Student's identity : Simon Ryckaert

Phelma's engineering program : international master nanotech / Filière nanotech

Academic year : 2024/2025

Title of the internship and period : Light trapping for single-junction solar cells and tandem solar cells, from March to August

Name and address of the Laboratory: Centre de Nanoscience et Nanotechnology (C2N/CNRS), 10 Bd Thomas Gobert, 91120 Palaiseau.

Name of supervisors and their mail addresses : Stephane Collin, [stephane.collin@cnrs.fr](mailto:stephane.collin@cnrs.fr) and Sylvain Finot, [sylvain.finot@ipvf.fr](mailto:sylvain.finot@ipvf.fr)

Description of the internship validated: The project consists of developing low-cost processes to trap light in ultra-thin solar cells, by studying and comparing innovative nano-metric structures to enhance the efficiency of silicon solar cells and tandem solar cells. The purpose of the internship will be, first, to model and simulate solar cells, and then to fabricate them.

Resources provided by the laboratory: OptiPV on Matlab, office, cleanroom (spin-coater, RIE ICP, RIE CCP, SEM, chemical hoods, AFM, reflectometer, lithography hoods).